DEVELOPMENT OF A WORKFLOW FOR ROBUST CYTOMETRY OF REACTION RATE CONSTANT

ROBEL YOSIEF

A THESIS SUBMITTED TO

THE FACULTY OF GRADUATE STUDIES

IN PARTIAL FULFILLMENT OF THE REQUIREMENTS

FOR THE DEGREE OF

MASTER OF SCIENCE

GRADUATE PROGRAM IN BIOLOGY

YORK UNIVERSITY

TORONTO, ONTARIO

August 2022

ABSTRACT

Cytometry of Reaction Rate Constant (CRRC) is a method for studying cell population heterogeneity based on the activity of cellular processes. The original CRRC workflow did not account for cell motility, which led to inaccurate measurements in motile cells. Here, we report on the development of a new CRRC workflow that makes it applicable to motile cells. We confirmed the robustness of the new workflow to cell movement by performing a comparative CRRC workflow study of cross-membrane transport in motile cells. Using the new workflow, preliminary progress was made on the investigation of cytochrome p450 (CYP) activity. We validated the CRRC experimental procedure to conduct such study but found that the CRRC CYP assay had considerable variability. Nonetheless, the development of the new CRRC workflow is a step in the right direction with more work needing to be done to understand the variability found in the CRRC CYP assay.

DEDICATION

To my beloved parents, Ruth and Yosief,

and my dear sister, Miriam, for

believing in me and for their unwavering

support

And to God for giving me strength and

guidance

ACKNOWLEDGEMENTS

I would like to thank every person who has assisted me in the completing of my thesis. First and foremost, I want to thank Professor Sergey N. Krylov for giving me the opportunity to be a part of his lab. He took a chance and accepted me into his lab although I did not have any prior research experience. In these two years, he has given me quality advice and taught me how to become a scientist. Thank you for the unforgettable experience you have provided me, Prof. Krylov.

Ideas were formulated and experiments were performed with the help of past and present members of the CRRC group. Firstly, I want to express my gratitude towards Dr. Vasilij Koshkin, the co-creator of the CRRC project with Prof. Krylov, who has been a source of vast knowledge and expertise for me. I also want to thank Giammarco Nebbioso, a close lab mate of mine who was inexperienced like me, for his great ambition, outgoing personality, and his attention to detail that has really pushed me. Aside from the project, Giammarco is someone I could talk to about anything, and I appreciate him for that. Finally, I want to acknowledge Dr. Mariana De Bleker Oliveira, who helped me during the first half of my studies. She taught me key components of the project and was very kind to me, which helped me find my place in the lab. To the rest of the Krylov lab members, I am thankful for all the assistance and scientific insight you have given me.

Lastly, I am grateful to Professor Chun Peng for the productive collaborations between the Krylov and Peng labs and for being a great supervisory committee member. She is warm and welcoming and gave me useful recommendations for the project during my research evaluations. From the Krylov-Peng collaboration, I must give a special thank you to Yumin Qui, a post-doctoral fellow, for providing cells to our lab and giving me valuable advice on cell culture. I could have not done this work without the support from Yumin, thank you so much.

TABLE OF CONTENTS

LIST OF TABLES

LIST OF FIGURES

LIST OF ABBREVIATIONS

A	Amplitude
ABC	ATP-binding cassette
ALDH	Aldehyde dehydrogenase
ATCC	American type culture collection
BCRP	Breast cancer resistance protein
BF	Brightfield
BRCA1/2	Breast Cancer Gene 1 & 2
CI	Confidence interval
CRRC	Cytometry of Reaction Rate Constant
CT	Computed tomography
CYP	Cytochrome p450
d	Mean cell diameter
DIC	Differential interference contrast
DNA	Deoxyribonucleic acid
ELISA	Enzyme-linked immunosorbent assay
FDA	Food and Drug Administration
FIM	Fluorescence intensity manager
FISH	Fluorescence in-situ hybridization
HBSS	Hank's balanced salt solution
HER2	Human epidermal growth factor
Il-Fld	Incident light field diaphragm
k	Rate constant
K_M	Michaelis constant
KRAS	Kirsten rat sarcoma virus
LAP	Linear Assignment Problem
LOG	Laplacian of Gaussian
MDR	Multi-drug resistance
ms	Milliseconds
MRI	Magnetic resonance imaging
mRNA	Messenger RNA
MRP1	MDR-associated protein 1
NADPH	Nicotinamide adenine dinucleotide phosphate
P-gp	P-glycoprotein
PBS	Phosphate buffered saline
PC	Phase contrast
PCR	Polymerase chain reaction
PET	Positron emission tomography
pH	Potential of hydrogen
PI	Propidium iodide
RSE	Relative standard error
RNA	Ribonucleic acid
RT- qPCR	Reverse transcription quantitative PCR
SD	Standard deviation

t_2	Time interval between subsequent BF images
Tau	Time constant
TD	Time offset
Tl-Fld	Transmitted light field diaphragm
v	Cell speed
V_{max}	Maximum reaction velocity
x	Shift in cell position
Yb	Baseline
y_0	Offset

INTRODUCTION

1.1 Chemoresistance

Chemotherapy is a long-established and routinely used cancer treatment that involves the administration of chemotherapeutic agents to target fast-dividing cells in patients.[1,2] Chemotherapeutic agents are either: *i*) cytotoxic or *ii*) cytostatic.[3] Cytotoxic agents inhibit cell division and cause cell death, while cytostatic agents slow or stop the growth of cells without killing them. An ongoing issue associated with chemotherapy treatment is when a patient displays chemoresistance, *i.e.*, tumour insensitivity to cytotoxic agents.[4] It is important to note that there are two types of chemoresistance: *i*) intrinsic and *ii*) acquired. Intrinsic chemoresistance is when the tumour is unaffected by the first application of chemotherapy.[5] Tumours can possess a subpopulation of cells that are inherently drug-resistant and cause cancer relapse after the first round of treatment. In contrast, acquired chemoresistance occurs when the tumour becomes insensitive to chemotherapeutic agents after the following rounds of treatment.[6] A tumour can respond positively to the first round of chemotherapy, but it will likely develop resistance during the course of treatment due to the appearance of new mutations or changes in the tumour microenvironment. For example, around 50% to 70% of ovarian adenocarcinomas will relapse within one year from the start of treatment.[7] Ultimately, chemotherapy will be unsuccessful in eliminating cancer for both forms of chemoresistance.

Evidently, chemoresistance is a concerning issue as it diminishes the effectiveness of chemotherapy leading to a shortened life expectancy of chemotherapy-treated cancer patients.[8] In fact, chemoresistance may be responsible for treatment failure for up to 90% of cancer patients.[9] This has been an inevitable situation for many years as chemotherapy was and still is a critical

component of cancer treatment, alongside radiation and surgery. However, alternative cancer treatments have been developed over the years, such as immunotherapy, hormone therapy, molecularly targeted inhibitors, signal transduction inhibitors, heat ablation, and cryotherapy.[10-14] Specifically designing a treatment regimen for an individual cancer patient, known as precision oncology, can avoid patients undergoing treatments later deemed to be ineffective and can improve the success of cancer treatment.[15] Thus, precision oncology is an innovative approach that has become a growing focus of cancer research.

1.2 Precision oncology cancer treatment model

Commonly, chemotherapy is one of the primary treatment options for a cancer patient and it involves the use of anticancer drugs that can be used by themselves or in combination with other anticancer drugs. If a patient is deemed to be chemoresistant, then alternative therapies are introduced.[16,17] However, it usually takes multiple rounds of chemotherapy before concluding a patient is chemoresistant, since one round of chemotherapy is usually insufficient for such conclusion. While the target of chemotherapy is fast-dividing cells, an inevitable side effect of chemotherapy is the destruction of healthy cells. The destruction of healthy cells can cause severe problems such as low blood cell counts, gastrointestinal disorders, hair loss, etc.[18] In addition, prolonged chemotherapy treatment potentially takes critical time away from the use of a more effective alternative therapy.

In the current cancer treatment model, patients would blindly undergo multiple rounds of chemotherapy without pre-therapeutic evaluation to determine whether a patient is chemoresistant or chemosensitive. Although this current cancer treatment model is frequently used, there may be a more effective cancer treatment model that involves precision oncology. This precision oncology based cancer treatment model would instead have pre-therapeutic evaluation to predict if the

patient would display intrinsic chemoresistance, so a decision can be made for the patient to undergo chemotherapy or an alternative therapy (**Figure 1**).[19] Having therapeutic evaluation prior to treatment could be extremely beneficial as it would potentially bypass unnecessary chemotherapy treatment and possibly lead to longer patient survival.[20] Predictive cancer biomarkers, specifically chemoresistance predictors, would be tested for in the pre-therapeutic evaluation to guide the decision of the most optimal treatment for the patient.
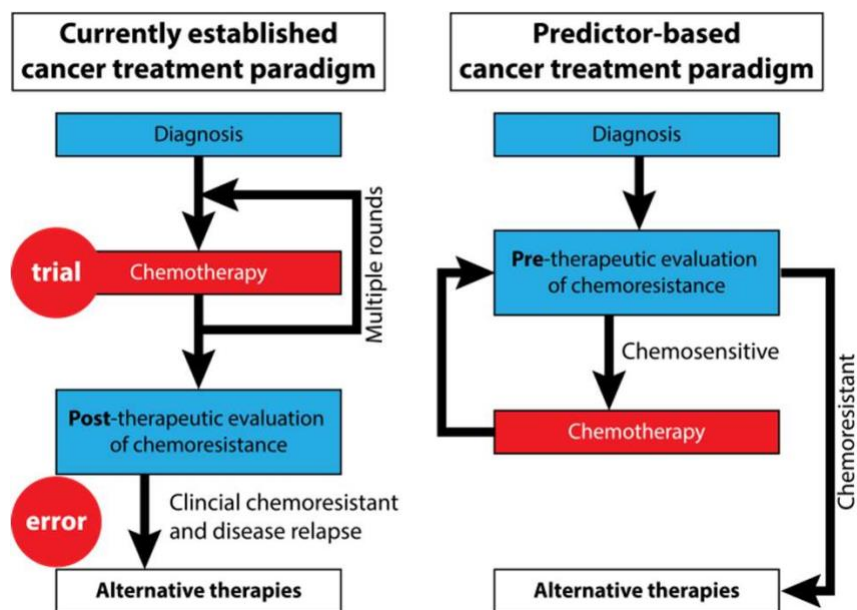
Figure 1. Comparison of the current and the precision oncology based cancer treatment paradigms. Blue boxes represent diagnostic and evaluation steps, while the red boxes represent the use of chemotherapy. The current cancer treatment model is a trial-and-error system, where multiple rounds of chemotherapy are required to determine chemoresistance. The precision oncology based treatment model involves pre-therapeutic evaluation to determine chemoresistance. Adapted from: Bleker de Oliveira M, Koshkin V, Liu G, Krylov SN. Analytical Challenges in Development of Chemoresistance Predictors for Precision Oncology. *Anal. Chem*. 09 2020;92(18):12101-12110. doi:10.1021/acs.analchem.0c02644.

1.3 Current state of chemoresistance predictors

Predictive cancer biomarkers are substances or processes measured in the body that can be used to predict a patient's response to a cancer treatment.[21] Specifically, chemoresistance predictors are a type of predictive biomarker that foresees a patient's response to chemotherapy.[22]

Thus far, many potential chemoresistance predictors have been proposed;[22-24] however, only a small portion of these potential predictors have been proven to be adequate for clinical use. In fact, only a few chemoresistance predictors have been approved by FDA.[25] Some examples of validated chemoresistance predictors are HER2 expression for breast cancer,[26] *KRAS* mutations for non-small cell lung cancer,[27] and high microsatellite instability for colorectal cancer.[28] Seemingly, there is a lack of suitable chemoresistance predictors as well as predictive biomarkers in general, which can be attributed to various reasons. These reasons include small study sizes leading to overestimation or underestimation of biomarker significance,[29] lack of coordination between biomarker research laboratories leading to poor reproducibility,[30] and the presence of regulatory and financial hurdles.[31]

1.4 Requirements of a chemoresistance predictor

A chemoresistance predictor associates a measurable clinical endpoint y which serves as an indicator of clinical chemoresistance, with a laboratory parameter x that is measured prior to chemotherapy treatment, via the function below:

$$F: y = F(x) \tag{1}$$

If y_{thres} is assigned as the threshold value that separates chemoresistance from chemosensitivity then a y value less than y_{thres} corresponds to chemosensitivity and y value greater than y_{thres} corresponds to chemoresistance. Graphical illustration of a chemoresistance predictor is shown in **Figure 2**.[19] Thus, measuring the laboratory parameter x before the treatment for an individual patient can be used to anticipate whether the patient has pre-existing chemoresistance.

To establish a chemoresistance predictor for clinical use, two fundamental requirements should be met. The first requirement is biological, there must be a strong biological relationship between the laboratory parameter and the clinical endpoint. The second requirement is technical,

4

the analytical methods used for measuring both the laboratory parameter and the clinical endpoint must be reliable in terms of precision, accuracy, robustness, and ruggedness. The failure to satisfy the technical requirement impacts the ability to correctly answer the question of whether there is a strong biological relationship between the lab parameter and the clinical endpoint, which would lead to questionable determination of chemoresistance. Hence, the analytical methods measuring the clinical and laboratory parameters should be first validated by testing their precision, accuracy, robustness, and ruggedness, in order to reliably determine chemoresistance.
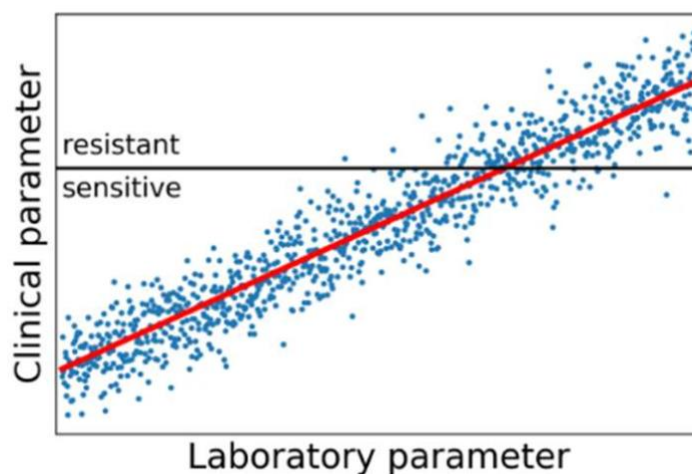
Figure 2. Graphical depiction of a chemoresistance predictor. A quantifiable clinical parameter is linked to a laboratory parameter measured from a patient prior to chemotherapy treatment. The y_{thres} value is designated as the threshold that distinguishes chemoresistance from chemosensitivity, so a y value less than y_{thres} corresponds to chemosensitivity and a y value greater than y_{thres} corresponds to chemoresistance. Adapted from: Bleker de Oliveira M, Koshkin V, Liu G, Krylov SN. Analytical Challenges in Development of Chemoresistance Predictors for Precision Oncology. *Anal. Chem.* 09 2020;92(18):12101-12110. doi:10.1021/acs.analchem.0c02644.

1.5 Analytical method validation parameters

It is important to understand what is meant by these four analytical method validation parameters: precision, accuracy, robustness, and ruggedness. These four key parameters are some of the many that are checked to ensure that a method is suitable for its intended reason and produces legitimate data.[32] The precision of an analytic method is the closeness of agreement between

measurements acquired under specific conditions.[33] In contrast, accuracy is the closeness of agreement between the value which is accepted either as the true or reference value and the measured value.[34] Robustness expresses the resistance of an analytical method to small, but deliberate variations in experimental settings and provides an indication of its reliability during routine use.[35] Lastly, ruggedness is the degree of reproducibility of results acquired by the analysis of the same sample under variable conditions, such as different laboratories, different analysts, different instruments, different analysis duration times, different analysis temperatures, different days, etc.[36] Thus, an analytical method can be considered reliable if it is shown to sufficiently precise, accurate, robust, and rugged.

1.6 Types of chemoresistance predictors

For this work, our focus is primarily on methods measuring laboratory parameters since methods for measuring clinical endpoints are considered satisfactory for correlation. A good example of a clinical endpoint that can be reliably measured because of its straightforwardness is overall survival, which is the length of time that a patient is alive from the start of the treatment or diagnosis.[23] For the methods that measure laboratory parameters, the majority of them fall short in at least one of the critical method validation parameters already discussed (precision, accuracy, robustness, ruggedness). Therefore, our analysis will discuss these methods that measure laboratory parameters and their analytical performance. Furthermore, we will classify chemoresistance predictors based on the type of method that measures the laboratory parameter. For simplification, the chemoresistance predictors that will be discussed are placed into four broad categories: *i*) whole-tumour properties, *ii*) genetic aberrations, *iii*) random screening for quantities of molecules, and *iv*) quantities or activities of relevant catalysts (**Figure 3**). The first category, whole-tumour properties, is the only type of predictor that uses non-biochemical analyses;

however, it has not shown much promise in clinical settings. The next two categories, genetic aberrations and random screening for quantities of molecules, are particularly useful for discovery of possible laboratory parameters that could be correlated to chemoresistance, since these two categories use wide screening methods. The last category, quantities or activities of relevant catalysts, is best used for validation of potential laboratory parameters linked to chemoresistance. Note that potential laboratory parameters are likely to have been identified from wide screening methods.

Figure 3. Classification of chemoresistance predictors based on lab parameters. Assessment of whole-tumour properties (red text) is the only non-biochemical analysis.

1.6.1 Whole-tumour properties

Theoretically, any quantifiable property of a whole tumour such as its size, vascularization, oxygenation, etc., can be used as a laboratory parameter to be linked with a clinical endpoint for the development of a chemoresistance predictor. Quantifying these tumour properties can be accomplished with non-invasive imaging techniques like ultrasounds, x-rays, magnetic resonance imaging (MRI), computed tomography (CT), and positron emission tomography (PET).[37] Chemoresistance predictors based on non-invasive imaging have been investigated in numerous cancers including breast,[38] ovarian,[39] and NSCLC.[40] However, no chemoresistance predictor based on tumour imaging has been successfully proven to be clinically useful.[41] Rather all the clinically used chemoresistance predictors are based on biochemical analyses of tissue or body fluid

specimens. Hence, the rest of the discussion of chemoresistance predictors will be centred around biochemical analyses.

1.6.2 Genetic aberrations

One type of biochemical chemoresistance predictor is based on genetic aberrations. Genetic aberrations are mutations, single-nucleotide polymorphisms, and chromosome deletions or translocations.[42] Many of these aberrations are measurable, so the percentage of tumour cells that carry a specific genetic aberration can be found.[43] Since these aberrations are simply listed as present or absent, they can be detected with high ruggedness, precision, accuracy, and robustness via DNA sequencing or fluorescence in-situ hybridization (FISH).[44,45] The simple recording of an aberration being present or absent seems to have low uncertainty, thus making it ideal for the development of chemoresistance predictors. However, it is important to note that a threshold for the percentage of cells that carry a genetic aberration must be set to determine whether a patient is positive or negative, which leads to controversy over interpretation of positivity.[46]

Although it appears to be an ideal laboratory parameter, there are only a few reliable chemoresistance predictors based on genetic abberations.[47] The two main issues hindering the genetic-based approach in producing more predictors are financial and biological. The first issue is financial, as the high cost for accurate whole-genome sequencing limits the amount of available data for predictor development.[48] It is noteworthy to mention that this financial barrier may be alleviated in the future with the development of more DNA sequencing technologies. Moreover, the second problem is concerned with fundamental biology since a single genetic abnormality usually does not tell a full story about drug resistance. Instead, there are many other levels of cellular regulation that can contribute to drug resistance such as epigenetic, transcriptional, and post-translational regulation.[49] Therefore, it is widely accepted that predictors based on genomic

aberrations are only useful for a small minority of cancer patients, but this approach may find more reliable predictors in the future with development of new DNA sequencing technologies.

1.6.3 Random screening for quantities of molecules

Another category of biochemical chemoresistance predictors is built upon the random screening for quantities of molecules. This category of predictor uses screening technologies to determine the abundance of mRNAs, proteins, post- translational modifications of proteins, miRNAs, metabolites, etc.[50,51] Molecules of interest are identified if there is correlation between the quantity of the molecule and a clinical endpoint. Thus, random screening for molecules of interest could potentially find a relevant laboratory parameter by chance, yet no approved predictors has been developed using this approach.

Measuring lab parameters for random screening predictors could be done through wide-panel hybridization assays, nucleic acid sequencing methods, mass spectrometry, etc.[30] All of these methods lack in either precision, accuracy, robustness, or ruggedness. For example, a microarray is a type of wide-panel hybridization assay that is semi-quantitative in nature. Microarrays have difficulties in accurately measuring absolute expression levels and detecting low abundance genes,[52] thus, it is inadequate for measuring a laboratory parameter. For nucleic acid sequencing, a popular method used is Nanostring, which can identify up to 770 gene transcripts in a single run by detecting mRNA molecules with target-specific probe pairs. [53] However, Nanostring is known to be irreproducible,[54] hence it cannot be used to ruggedly measure a lab parameter. Other methods, such as RT-qPCR and ELISA, are commonly used for quantitative measurements of small sets of molecules identified from the wide screens.[55,56] But, RT-qPCR and ELISA have their own flaws such as the requirement for complex extraction of molecules of interest in RT-qPCR,[57] and non-specific antibody binding leading to a high background signal in ELISA.[58] Moreover, RNA-Seq is

a highly accurate technique that can determine the differential expression of genes and transcripts with minimal amounts of RNA.[59] Although RNA-Seq is highly accurate, there are struggles associated with sample preparation as low quality or quantity of recovered RNA causes biased results for this technique.[60] Collectively, random screening methods are suitable for identification of prospective molecules of interest, but these methods lack in either precision, accuracy, robustness, or ruggedness for measuring these molecules of interest for chemoresistance prediction.

1.6.4 Quantities or activities of relevant catalysts

Contrary to the predictors that rely on random screening for molecules of interest, there are other predictors that focus on relevant cellular processes that are known beforehand to be involved in chemoresistance. Most cytotoxic drugs inflict DNA damage in rapidly-dividing cells and subsequently trigger apoptosis in these cells, killing these cells. The cytotoxic effect of these drugs can be hindered when tumour cells display chemoresistance. Three common scenarios of chemoresistance are when: (*i*) the drug is expelled from the cells before reaching the nucleus, (*ii*) the drug cannot induce DNA damage because it is inactivated by drug-metabolizing enzymes, (*iii*) the drug reaches the nucleus and induces DNA damage; however, the DNA damage is quickly repaired by DNA repair enzymes, therefore apoptosis is prevented. These three chemoresistance mechanisms (drug expulsion, drug inactivation, and DNA damage repair) are directly linked to cytotoxic drugs, unlike other chemoresistance mechanisms, such as increased cell survival and inhibition of apoptosis. Furthermore, these three mechanisms are catalyzed by transporters or enzymes, hence, the amount or activities of these catalysts could be quantified for use as lab parameters.

1.6.4.1 Quantity of catalysts vs. their activity

Lab parameters of chemoresistance mechanism based on drug extrusion, drug degradation, or DNA damage repair can either be based on the amount or the activity of the catalyst. For an abundance-based lab parameter, the quantity (expression) of the catalyst is measured by the amount of mRNA or protein of that catalyst. Measuring mRNA or protein levels can be conveniently done within an affinity assay (hybridization assay or immunoassay), such as RT-PCR or Western blot. Nevertheless, the amounts of mRNA or protein of the catalyst does not correlate to the actual rate of catalysis, which is dependent on many other factors. Some factors include post-transcriptional and post-translational regulation, such as alternative splicing and post-translational protein modifications.[61] Moreover, expression assays are inadequate for characterization of catalysis due to the influence of the tumour microenvironment on the reaction rate of transporters.[62] Consequently, the expression levels of catalysts are unreliable lab parameters that are unlikely to correspond with clinical endpoints. On the other hand, the activities of a catalysts may provide a stronger basis for a chemoresistance predictor. There are different ways to analyze the activity of a catalyst as shown in **Figure 4.** The next sections will focus on the measurement of catalyst activities.
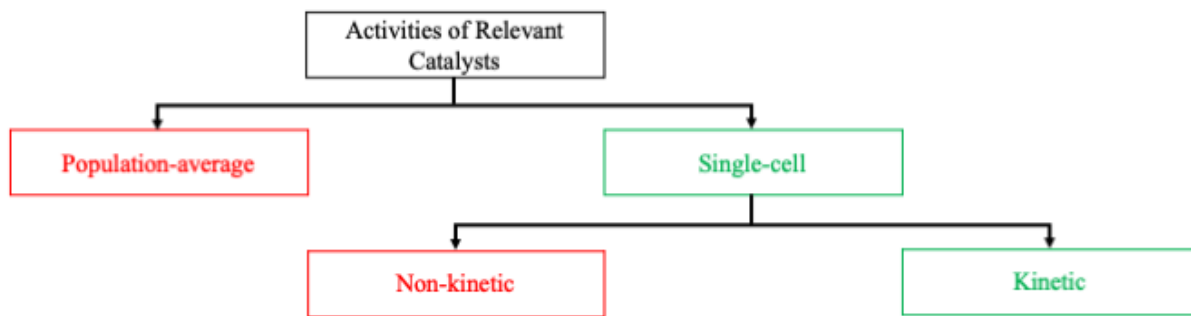
Figure 4. Different methodological approaches to analyze the activity of a catalyst. Green text indicates our preferred approach (a single-cell kinetic assay), as explained in the following sections.

1.6.4.2 Population-average vs. single-cell approaches

The activities of catalysts are either investigated at the population or the single-cell level. Using the population approach, an average of a measurable characteristic is taken and used to describe the whole cell population. Taking the population average would be unfavourable for tumours. As we know, tumours are inherently heterogenous, meaning they comprise of cells that differ in many ways such as their morphology, gene expression, and the activities of cellular reactions.[63] Accordingly, taking the population-average would ignore an important feature of tumours, which is their heterogeneity.

In consequence, population-average approaches would be unable to identify a drug-resistant cell subpopulation that exhibits increased activity of MDR transporters, drug-metabolizing enzymes, or DNA damage repair enzymes. Not knowing the size of the drug-resistant cell subpopulation is potentially detrimental, since the size of this specific cell subpopulation is connected to chemoresistance; with a greater number of drug-resistant cells in the tumour, there is a higher chance that some cells would survive chemotherapy and cause cancer relapse.[64] Evidently, the only way to accurately determine the size of a drug-resistant cell population is through a single-cell assay. Single-cell assays analyze individual cells from a large cell population and can, accordingly, identify a subset of cells that are drug-resistant. If the size of the drug-resistant cell population is accurately measured, it can then be utilized as a lab parameter to be correlated with a clinical endpoint. Generally, the measurement of the number and characteristics of individual cells is termed cytometry.

1.6.4.3 Non-kinetic vs kinetic approaches for assessing catalyst activity

Cytometry techniques that assess the activities of cellular processes at the single-cell level are either non-kinetic or kinetic. A non-kinetic cytometry technique, such as measuring the amount

of fluorescent product formed at a specific time point, can be used in theory to obtain reaction rates leading to the characterization of a drug-resistant cell subpopulation. However, there is a glaring issue with robustness regarding non-kinetic cytometry, since a small variation in the substrate concentration may significantly influence the results leading to different determined reaction rates. Consequently, non-kinetic cytometry techniques are non-robust and cannot be reliably used to characterize the size of a drug-resistant cell subpopulation.[65]

An example of a commonly used non-kinetic cytometry technique is flow cytometry.[66] Flow cytometry can differentiate cells within a large, heterogenous population by measuring physical and chemical properties of individual cells as they are forced to pass through a laser beam in a single-file line. The problem with flow cytometry for assessing the activities of catalysts is that measurements cannot be repeated, since cells can only pass through the laser beam once. Considering reactions do not occur instantly, multiple measurements must be taken during the reaction itself to truly assess the activities of catalysts. Most single-cell assays that use flow cytometry have already been proven to be inaccurate and non-robust.[67] Therefore, flow cytometry is a non-kinetic technique that is inadequate to determine the activities of catalysts to distinguish a drug-resistant cell subpopulation.

Thus, a kinetic cytometry technique is required to accurately assess the activities of catalysts for characterization of a drug-resistant subpopulation. Now, the question is what kinetic measurement can be used for this assessment of catalytic activity. Fundamentally, a chemical reaction is the process of reactants transforming into products and catalysts are substances that increase the reaction rate without being consumed.[68] An accurate quantitative descriptor of a chemical reaction is the reaction rate constant, k, which relates the concentrations of the reactants to the reaction rate. Importantly, the rate constant is also a robust quantitative parameter, meaning

that it is insensitive to minimal changes in experimental settings, such as the substrate concentration and the duration of experiment. Moreover, rate constants can be measured at the single-cell level to quantify the activity of catalysts involved in the established chemoresistance mechanisms (drug expulsion, drug metabolism, and DNA damage repair) for accurate and robust determination of the drug-resistant cell subpopulation.

1.7 Introduction to Cytometry of Reaction Rate Constant (CRRC)

Here, we introduce a kinetic cytometry technique that measures rate constants to characterize cell population heterogeneity, called the "Cytometry of Reaction Rate Constant" (CRRC).[65,69-73] CRRC is a method based on time-lapse fluorescence microscopy and can be summarized in five major steps (**Figure 5**).[65] First, a fluorescent or fluorogenic (initially non-fluorescent) substrate that is involved in the mechanism of interest is loaded into the cells. Then, fluorescent images of many cells are acquired progressively to follow the changes in intracellular fluorescence intensity. The images are processed to generate kinetic traces (intracellular fluorescence intensity *vs.* time) for each cell. Next, single-cell rate constants are calculated from exponential fitting of the kinetic traces. Lastly, the rate constant distribution is shown as a kinetic histogram (number of cells *vs.* rate constant).
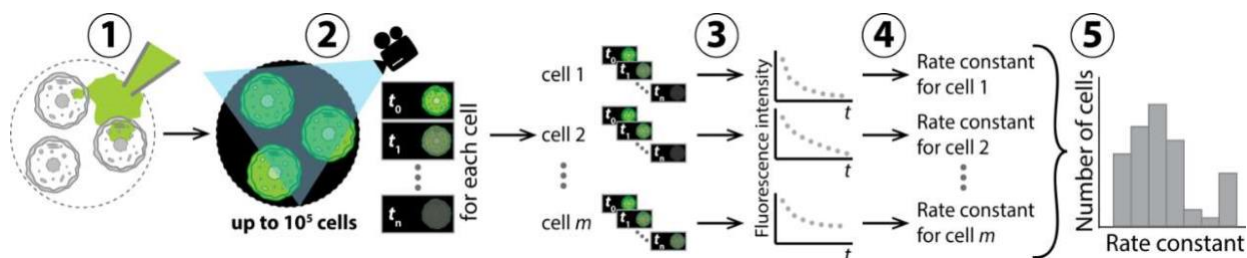
Figure 5. Schematic representation of CRRC. See text for details. Adapted from: Koshkin V, Kochmann S, Sorupanathan A, et al. Cytometry of Reaction Rate Constant: Measuring Reaction Rate Constant in Individual Cells To Facilitate Robust and Accurate Analysis of Cell-Population Heterogeneity. *Anal Chem*. 03 2019;91(6):4186-4194. doi: 10.1021/acs.analchem.9b00388.

1.7.1 MDR transport activity analysis by CRRC

So far, the main mechanism investigated by CRRC has been drug extrusion facilitated by MDR transporters. MDR transporters are predominantly responsible for extrusion of drugs, including chemotherapeutics, thus, they contribute to chemoresistance in various cancers such as breast, ovarian, and colorectal cancer.[74] MDR transporters are ATP-dependent and transport a substrate against its concentration gradient.[75] There are many MDR transporters, but there are three isoforms that are heavily linked to chemoresistance: P-glycoprotein (P-gp), MDR-associated protein 1 (MRP1), and breast cancer resistance protein (BCRP).[76] The activity of these transporters can be simply assessed with fluorophores, which are non-specific for the different MDR transporters.[77] In studies of MDR with CRRC, a fluorophore (fluorescein) and MDR transporter inhibitor (glyburide) is loaded into the cells and allowed to accumulate in the intracellular space. Consequently, after the removal of the MDR transport inhibitor, the decrease in intracellular fluorescence is followed over time as an indicator of the transporters' activity.

In previous work, CRRC was shown to be robust and accurate in studying cell population heterogeneity based on the activity of MDR transporters,[78] and that it can differentiate cell subpopulations with low and high k_{MDR} constants.[79] In addition, it was shown that many phenotypes do not alter significantly in the first 96 hours after dispersion of cells from three-dimensional clusters,[80] suggesting that the rate constant measured in dispersed cells can be used for analysis of MDR activity in solid tumors, from which the dispersed cells originated from. Furthermore, it was demonstrated that dispersed cells acquired by disintegration of three-dimensional clusters preserve their MDR activity for 24 hours.[81] Altogether, these results suggest that CRRC can reliably measure the activity of a MDR-mediated drug extrusion for identification of a drug-resistant population.

1.7.2 Identification of cell motility issue with original CRRC protocol

CRRC is a method that is still in its infancy stage of development and requires considerable efforts until it is ready to be used in clinical practice. In clinical practice, CRRC will be used to analyze primary cells derived from a tumour, but first, it must produce reliable and consistent results for cell lines. We studied the activities of xenobiotic-metabolizing enzymes, cytochrome p450 (CYP) and aldehyde dehydrogenase (ALDH), for the first time and obtained irreproducible and non-robust results in various cell lines such as MCF7 (breast cancer) and OVCAR3 (ovarian cancer). After carefully examining the images obtained, we found that some cells would move during the experiment, even though cells were attached to the cell culture plate surface. An example of cell motility is shown in **Figure 6**. Since we assumed cells would remain stable for the entirety of the experiment, cell motility was completely disregarded in our original CRRC protocol. In addition, unintentional shifts caused by the manual addition of the fluorogenic substrate or nuclei stain, propidium iodide (PI), to the cell culture plate would also cause cells to lose their position. Thus, it became clear that a new CRRC workflow that addresses cell motility had to be developed, in order to obtain reliable measurements.
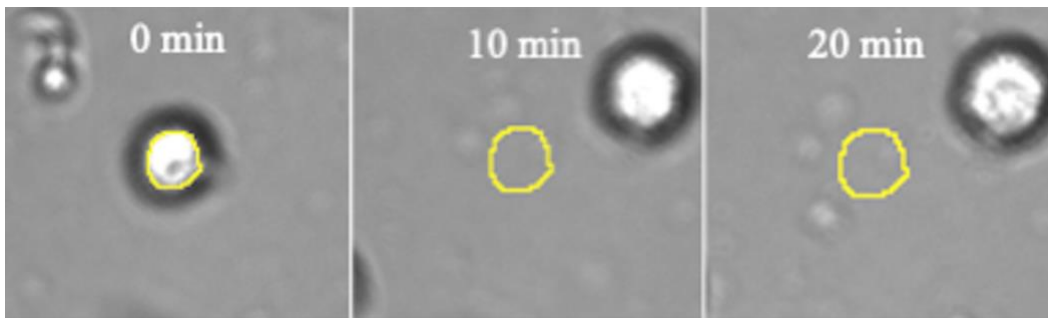
Figure 6. An example illustration of a motile OVCAR3 cell. The yellow outline is the identified cell contour at time zero. As time passes, the cell moves from the identified cell contour at time zero, indicating that cell is moving from its starting position.

<h1>Chapter Two</h1>

<h1>DEVELOPING A WORFKLOW FOR CYTOMETRY OF REACTION RATE CONSTANT (CRRC) THAT ADDRESSES CELL MOTILITY</h1>

The presented material is a manuscript titled "Workflow for Cytometry of Reaction Rate Constant (CRRC) to be Applicable to Motile Cells" that is currently under review and pending publication.

My contributions to the manuscript were: *i*) developing the new workflow, *ii*) performing all presented experiments, *iii*) interpreting results, *iv*) preparing figures, and *v*) writing and editing the manuscript.

2.1 Background

Cell tracking has become an essential component of live-cell experiments that involve time-lapse fluorescence microscopy.[82-84] The original CRRC workflow did not account for cell motility, since all cells were assumed to remain in the same position during the time-lapse experiment. In the original workflow, cells were stained with PI and a fluorescence image was taken to reveal cell positions at the end of the experiment. Hundreds of cell contours would then be manually drawn on the PI-stained image by the analyst and these cell contour masks were used to determine intracellular fluorescence intensities for the entire stack of images. Evidently, the results of CRRC will be inaccurate for motile cells because the "static" cell contours used to determine intracellular fluorescence will not follow the continually changing cell positions. Thus, making CRRC insensitive to cell movement requires a revamped workflow that finds cell contours for each image and follows these cell contours through the image stack.

Our new CRRC workflow combines two optical microscopy techniques: (*i*) transmitted-

light microscopy for cell-contour identification and cell tracking through the time-stack of images and (*ii*) fluorescence microscopy for monitoring intracellular fluorescence intensities. To acquire images, our microscope is configured to automatically take a transmitted light image before every fluorescence image. Stacks of matching fluorescence and transmitted-light images are then processed and analyzed automatically to extract kinetic traces "intracellular fluorescence intensity *vs* time".

2.2 Justification for use of transmitted-light microscopy

To ensure robustness of CRRC to cell movement, cell contours must be identified in the fluorescence images. This cannot be solely accomplished with imaging substrate conversion into the fluorescent product or imaging extrusion of the fluorophore since some images in the CRRC experiment will have too low of a fluorescent signal to distinguish cells from the background. Substrate conversion into fluorescent product causes a fluorescence increase, but the beginning images in the CRRC experiment will have minimal fluorescence for cell contours to be identified. The same concept applies to extrusion of the fluorophore which causes fluorescence decrease, then the last images of the experiment will have too low of a fluorescent signal for cell contour identification. Hence, it appears that the only practical way of identifying cell contours in the fluorescence images monitoring the reaction of interest in CRRC is to adopt a multichannel imaging approach.

The multichannel imaging approach entails acquiring an accompanying image that can either a be another fluorescence image or a transmitted-light one. Using an accompanying fluorescence image requires staining cells with a fluorescence probe spectrally distinct from the fluorescent product or fluorophore. Such a probe would introduce unnecessary chemical stress on the cells and could also interfere with determination of the product's fluorescence intensity due to

inevitable spectral overlaps. Therefore, we would prefer to use an accompanying transmitted-light image that avoids these potential issues. Further, modern microscopes have the capability to have separate focusing for different imaging modes, as the focal planes for fluorescence and transmitted-light modes may differ.

Normally, transmitted-light images are not used for cell-contour identification, since the contrast between cells and background in transmitted-light images is insufficient. Moreover, automated cell contour recognition software is usually designed for fluorescence images, as cells appear as bright spots on a dark background in these images. The easier a cell could be recognized by the human eye will lead to better cell contour recognition performance. Standard transmitted-light images, such as BF, DIC, and PC, do not provide the desired contrast like a fluorescence image, thus, these transmitted-light images need to be modified to have enhanced contrast. Various methods exist for increasing transmitted-light image contrast for cell contour identificaiton.[85-88] We chose to use a method called thresholding for its straightforwardness and its availability as a software tool for most modern microscopes. Thresholding is limiting the pixel intensities of an image to a small range, so that pixel intensities above the selected range convert to white (bit value of 1) and pixel intensities below the lower limit of the range convert to black (bit value of 0). Further, it was demonstrated that thresholding benefits from having a transmitted-light image slightly out of focus.[87] The result of thresholding is a high-contrast transmitted-light image, where the cells appear as a bright spots on a dark background. An example of thresholding for a brightfield image is shown in **Figure 7**. It is important to state that raw DIC and PC images have inherently better contrast than BF, therefore they should outperform BF in cell contour identification. However, it is questionable if DIC and PC retain this advantage after undergoing thresholding, thus, a comparison between the three transmitted-light modes is required.
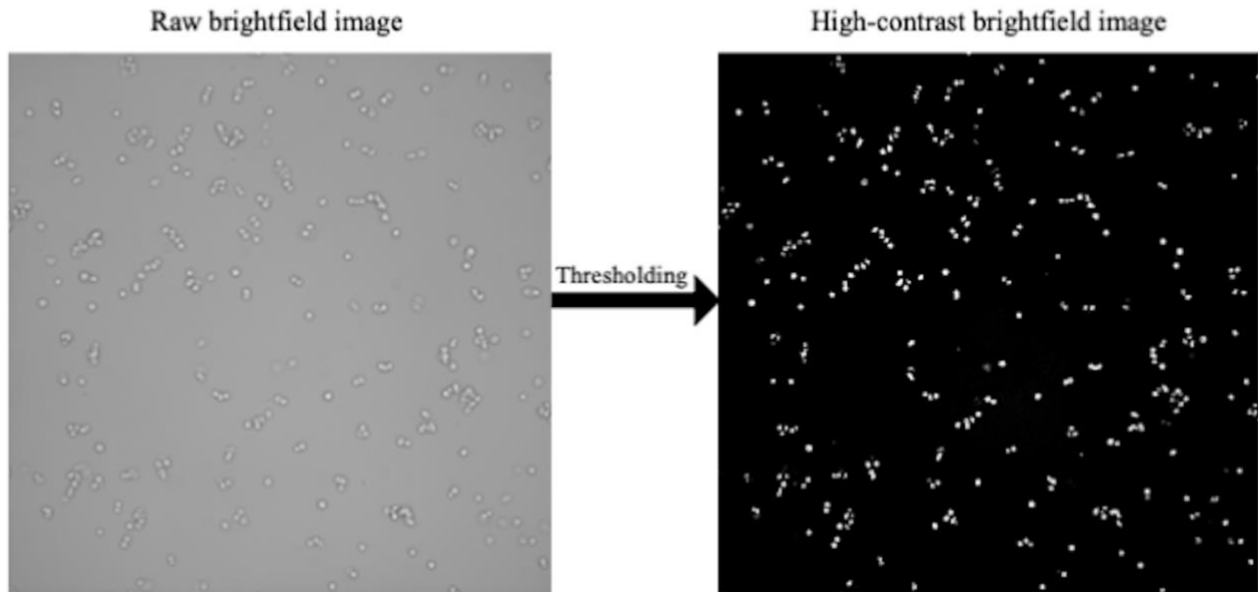
Figure 7. Example of using thresholding to enhance contrast for a brightfield image. On the left is a raw brightfield image out of focus by 30 μm, which undergoes thresholding to produce a high-contrast version of the same image on the right.

2.3 Experimental layout

Our experimental layout for the development and validation of the new workflow involved five major steps. First, we compared the three transmitted-light modes for their cell contour identification performance and found that BF performed best using the thresholding technique, thus, BF was chosen as the transmitted-light image in the new workflow. Second, we tested the cell area determination ability of the altered BF images and found that they underestimate cell area; however, we proved this underestimation of cell area does not affect the results of CRRC. Third, we confirmed that cell movement between a matching fluorescent and BF image is negligible even for highly-motile cells; hence, the cell contours found for BF images are applicable to fluorescence images. Fourth, we performed an experiment for microscopes that are unable to separately focus for multichannel imaging and proved that the new workflow is insensitive to the difference in focal planes between the BF and fluorescence images. Finally, we compared the

original and new workflows of CRRC by investigating cross-membrane transport in motile cells. We found that the original workflow tends to overestimate rate constants causing a shift of the histogram to the right, while the new workflow was unaffected by cell motility.

2.4 Materials and methods

2.4.1 Cell culture

Ovarian cancer cells TOV-112D were acquired from ATCC and grown in MCDB 105/Medium 199 (Sigma-Aldrich, St. Louis, MO, USA, Cat. No. of MCDB 105: M6395, Cat. No. of Medium 199: M5017) supplemented with 10% fetal bovine serum (Gibco, Grand Island, NY, USA, Cat. No: 12483-020). Cells were cultured in 60 mm plastic-bottom dishes (Sarstedt AG&Co, Numbrecht, Germany, Cat. No: 83.3901), 35 mm plastic-bottom dishes (Nest Biotechnology Co, Wuxi, Jiangsu, China, Cat. No: 706001), and a 50 mm glass-bottom dish (Mattek, Ashland, MA, USA, Cat. No: P50G-1.5-14-FGRD). The 35 plastic-bottom dishes were used for imaging except for one exception in the "Deciding on which transmitted light microscopy technique to use" section where a 50 mm glass-bottom dish was used. Cells were cultured at 37°C in a humidified incubator with 5% CO_2 until they reached 70% confluency.

2.4.2 Cell staining

PI-nuclei staining was conducted for cell counting and to reveal cell positions after completion of the time-lapse experiment in original workflow. To perform PI-nuclei staining, 10 µL of 6.5 mM saponin (Sigma-Aldrich, St. Louis, MO, USA, Cat. No:8047152), a cell membrane permeabilizing agent, and then 5 µL of 1 mM propidium iodide (PI, Sigma-Aldrich, St. Louis, MO, USA, Cat. No:25535164) were added into the cell culture plate containing 1.2 mL of Hanks' Balanced Salt Solution (HBSS) (Gibco, Grand Island, NY, USA, Cat. No:14025092).[89] After 10 minutes, cells were imaged without washing. For experiments that required cytoplasmic staining,

cells were treated with 2 µM DRAQ9™ (Novus Biologicals, Littleton, CO, USA, Cat. No: NBP2-81128) in HBSS. After 30 minutes, cells were washed three times with PBS (Cytiva, Logan, Utah, USA, Cat. No: SH30256.01) and then imaged.

2.4.3 New CRRC experimental protocol for cross-membrane transport

The full CRRC cross-membrane transport experiment involved the following four steps. First, we removed the cell culture medium and washed cells once with 1 mL of PBS. Second, we added a 1.2 mL HBSS solution containing 1.5 µM fluorescein (Sigma-Aldrich St. Louis, MO, USA, Cat. No:518478), the substrate of cross-membrane transport, and 10 µM glibenclamide (Research Biochemicals International, Natick, MA, USA Cat. No: G106), a multidrug resistance transport inhibitor, to the cell culture plate and incubated cells for 30 minutes. Third, we removed the substrate and inhibitor containing HBSS solution from the cell culture plate, and washed cells three times with 1 mL of PBS. Fourth, we added 1.2 mL of pure HBSS to the cell culture plate and then started image acquisition with alternating fluorescence and BF modes every 1 minute for 1 hour.

2.4.4 Image acquisition

In previous CRRC studies, imaging was only performed with confocal laser-scanning fluorescence microscopy.[65,81,90] Here, we used epifluorescence microscopy with a Leica DMi8 high-throughput cell-imaging system. This imager is capable of fully automated time-lapse image acquisition with alternating imaging modes, such as fluorescence and transmitted-light microscopy. The "Relative Focus Correction" feature of the imager was used to set different Z-positions between the alternating imaging modes. All images were acquired with a 10× objective lens and the fluorescence of intracellular fluorescein was excited with a blue light-emitting diode. A FITC filter cube was used for fluorescein, RHOD cube for nuclei stain PI, and a Cy5 cube was

used for cytoplasmic stain DRAQ9. For transmitted-light microscopy, BF and DIC images were acquired with the same 10× apochromatic objective lens as fluorescence (HC PL APO 10x/0.45). PC images were acquired with a N Plan 10×/0.25 PH1 objective lens. All images were captured with a deep-cooled high resolution sCMOS camera. To acquire images of multiple regions of the cell culture plate, the "Mark and Find" option of the microscope was enabled.

2.4.5 Image settings

The following are the image settings for each Figure. For **Figure 8**, BF: no binning, 7.81 ms (milliseconds) exposure, high well capacity, intensity 48, aperture 7, transmitted light field diaphragm (Tl-Fld) 23, 196–191 intensity threshold. DIC: no binning, 7.81 ms exposure, high well capacity, intensity 128, aperture 15, Tl-Fld 46, bias 50, 192–192 intensity threshold. PC: no binning, 7.81 ms exposure, high well capacity, intensity 130, aperture 24, Tl-Fld 23, 129–128 intensity threshold. Fluorescence: RHOD channel, no binning, 50 ms exposure, low noise, fluorescence intensity manager (FIM) 30%, incident light field diaphragm (Il-Fld) 6. For **Figures 9 and 13**, BF: no binning, 7.81 ms exposure, high well capacity, intensity 48, aperture 7, Tl-Fld 23, 196-191 intensity threshold. Fluorescence: Y5 channel, 2×2 binning, 50 ms exposure, low noise, FIM 30%, Il-Fld 6. For **Figures 10, 15, and 16**, BF: no binning, 7.81 ms exposure, high well capacity, intensity 38, aperture 12, Tl-Fld 46, 196–191 intensity threshold. Fluorescence: FITC channel, no binning, 7.81 ms exposure, low noise, FIM: 30%, Il-Fld 6. For **Figure 11**, BF: no binning, 8 ms exposure, high well capacity, intensity 48, aperture 11, Tl-Fld 46, 84–80 intensity threshold.

2.4.6 Image processing in Fiji

We used Fiji, an open-source software often used by biologists, for image processing and image analysis.[91] Once the stacks of fluorescence and brightfield images were acquired, they

were placed in Fiji and combined as one composite channel. Then, the composite channel was loaded onto a recent version of TrackMate,[92] a plugin built for cell identification and tracking. In TrackMate, automated cell contour identification was performed for the brightfield images using the StarDist dectector.[93] From the identified cell contours, cells were tracked with the Linear Assignment Problem (LAP) tracker. For tracking, the maximum distance allowed that cells could travel between frames was set to diameter of a large cell (~ 20 µm) to ensure the same cell is followed in the track. Moreover, cells that did not have full-length tracks were excluded from further analysis. Lastly, using the cell tracks generated from the brightfield images, intracellular fluorescence intensities were extracted from the fluorescence images.

2.4.7 Formation and analysis of kinetic traces

The intracellular intensities extracted from TrackMate were arranged on Microsoft Excel to form individual kinetic traces. The kinetic traces were inputted in OriginPro®, a data analysis and graphing software, and exponentially fitted with the "ExpDec1" for calculation of the rate constant, k_{efflux}. The "ExpDec1" function is shown below:

$$y = y_0 + Ae^{-\frac{x}{Tau}} \tag{2}$$

where y_0 = offset, A = amplitude, Tau = time constant, and k_{efflux} (decay rate) is a derived parameter = $1/Tau$.

Note that in previous CRRC studies, we obtained a rate constant characterizing the activity of only ATP-binding cassette (ABC) transporters, k_{MDR}. Now, we decided to obtain a rate constant for total substrate efflux, k_{efflux}. The two reasons for this change were: *i*) total drug extrusion of cross-membrane transport may be a better descriptor of drug resistance than drug extrusion catalyzed by ABC transporters only and *ii*) it is simpler to perform CRRC for determination of k_{efflux} instead of k_{MDR}. Furthermore, the following k_{efflux} values were removed from further analysis:

k_{efllux} values obtained from unsuccessful fitting, negative k_{efflux} values, and k_{efllux} values with high uncertainty (relative standard error, RSE > 100%).

2.4.8 Cell population analysis

Cross-membrane transport of each cell population determined by the original and new workflows were characterized by frequency histograms of cellular k_{efflux} values. In OriginPro, histograms were plotted using the "Custom Binning" mode, while the median (peak position) and skewness (peak asymmetry) values of the k_{efflux} distributions were obtained using the "Descriptive Statistics" tool. The k_{efflux} distributions were compared using the two-sample Kolmogorov-Smirnov test, considering $\alpha = 0.001$ as the criterion of statistical significance.

2.5 Results and discussion

2.5.1 Deciding on which transmitted light microscopy technique to use

The preference between the three transmitted-light modes was decided by their performance in correctly identifying cells. To determine the reference value for an accurate cell count, we manually counted PI-stained cells in a fluorescence image. We used this image for reference because PI-stained cells appear as well-distinguished bright spots, since neighbouring nuclei are spaced out by cytoplasm. Therefore, PI-stained fluorescence images are highly suited for both manual cell counting and cell counting software.[94] An example of a raw fluorescence image of PI-stained cells is shown in the leftmost panel of **Figure 8A**. After taking the fluorescence image, we took BF, DIC, and PC images of the exact, same region of the cell culture plate as the fluorescence image. Note that the transmitted-light images were taken 30 µm lower than their focal plane, so that cells appear brighter than the background, which aids in thresholding (see three rightmost panels in **Figure 8A** as an example).

All four types of raw images (fluorescence, BF, DIC, and PC) were processed before

automated cell contour identification took place. The fluorescence images were converted from RGB to the 16-bit format and the background in these images were subtracted by 50 pixels using the "rolling ball radius" algorithm (see the leftmost panel in **Figure 8B** as an example). Transmitted-light images underwent live-mode thresholding to obtain high-contrast images (see three rightmost panels in **Figure 8B** as an examples). The cells were then counted in all four high-contrast images for multiple regions of the cell culture plate using the cell contour determination software (StarDist). A radius range filter (3 to 12 µm) was applied to ensure that we only counted single cells and excluded cell debris and clustered cells which could not be distinguished. The obtained cell numbers were compared to the reference manual count.
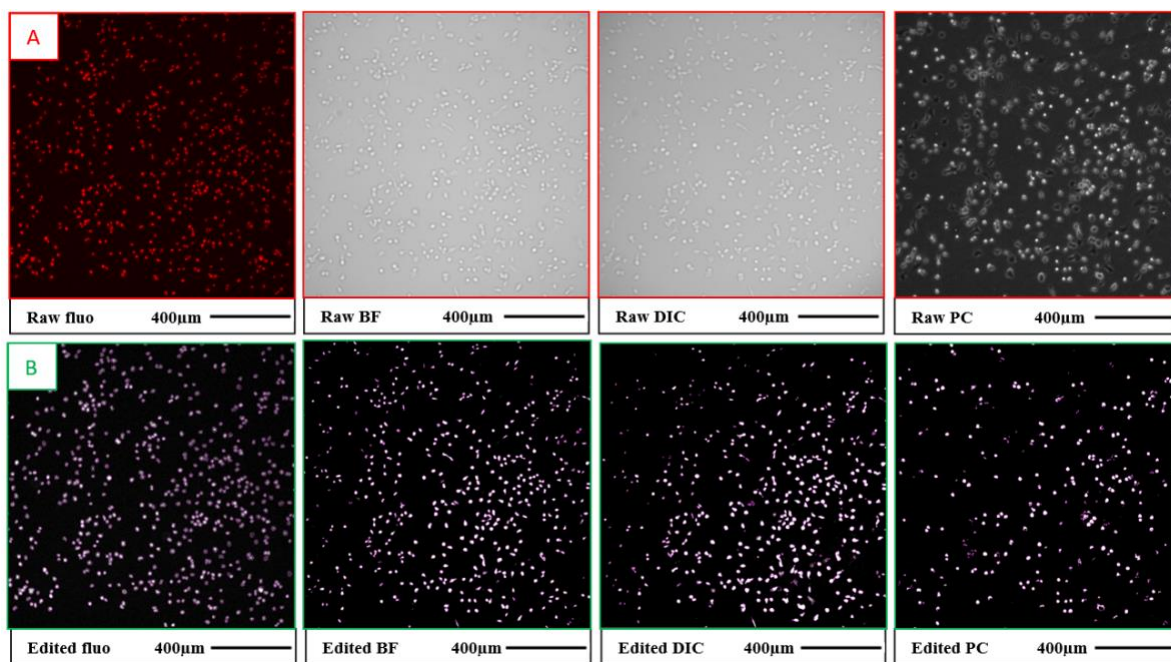
Figure 8. Comparing three modes of transmitted light-microscopy (BF, DIC, and PC) in their cell contour identification performance of TOV-112D cells on a plastic-bottom dish. The highest percentage of correctly identified cells was considered the winner for this competition. **Panel A** (red contours) shows raw, unmodified images. Cells were manually counted in the fluorescence (fluo) image of PI-stained cells and this number was used as reference (583 in this example). The fluorescence image was in-focus, while the three transmitted-light images were out-of-focus to facilitate thresholding for enhanced contrast. **Panel B** (green contours) shows the resulting images from thresholding with the identified cell contours (magenta). The raw fluorescence image was converted from RGB to 16-bit format and the background of the image was subtracted using the "rolling ball radius" algorithm (50 pixels). The raw transmitted light images were subjected to thresholding and converted to the 16-bit format. In this example, the percentages of correctly identified cells were: 96% in the edited fluorescence image, 88% in the edited BF image, 79% in the edited DIC image and 43% in the edited PC image.

A consideration we took in the cell counting results is that DIC imaging of cells is usually done on a glass-bottom dish,[95] due to plastic being a birefringent material that can cause optical disturbances with DIC. Thus, we conducted a comparative study of the transmitted-light modes in their ability of correctly identifying TOV-112D cells grown on both plastic (30-mm) and glass-bottom (50-mm) dishes. For the plastic-bottom dish, we found that the mean percentage of cells (standard deviation [SD]) that the software could identify were 98% (1%), 83% (5%), 68% (8%), and 47% (4%) in fluorescence, BF, DIC, and PC images, respectively (mean and SD were calculated over three regions). For the glass-bottom dish, we found that the mean percentage of identified cells (SD) that the software could identify were 99% (1%), 75% (7%), and 70% (5%) in fluorescence, BF, and DIC images, respectively (mean and SD were calculated over five regions). Although the software identified 74% (7%) of cells in PC images on a glass-bottom dish, it was evident that almost all identified cells had incorrect contours due to a pronounced halo effect that occurs with PC microscopy.[96] Thus, PC on glass-bottom dishes was removed from any further consideration.

The highest percentage of correctly identified cells was expectedly obtained for the fluorescence mode. This result was unsurprising since cell recognition software is made for fluorescence images, since this type of image naturally provides excellent contrast for cells without any enhancement required, as mentioned before. For the transmitted-light modes, BF had the highest percentage of correctly identified cells both on a plastic-bottom (83%) and glass-bottom dish (75%), thus it was considered the winner in our competition and was used as the transmitted-light mode for cell contour identification and cell tracking in our new workflow.

2.5.2 Cell area determination

Although BF was considered the winner from the transmitted-light modes for cell counting,

we also wanted to test its performance in cell area determination. To accomplish this, we took fluorescence images of TOV-112D cells stained with cytoplasmic dye DRAQ9 and then took BF images of the same field of views and compared the mean cell area in the BF images to the fluorescence images (**Figure 9**). Again, the radius range filter (3 to 12 µm) was applied to ensure that we only obtained the areas of single cells. We found that mean cell area (SD) in the cytoplasm-stained images was 176.66 µm^2 (3.31 µm^2), while the mean cell area was 94.31 µm^2 (2.68 µm^2) for the BF images (mean and SD were calculated from three fields of view). These results correspond to a deviation of 46.62% between the determined mean areas from the fluorescence and BF images, with the BF images clearly underestimating the cell area. This result was unsurprising as thresholding in the BF images can cause parts of the peripheral cell area to be removed. However, there may be overestimation of cell area in the fluorescence image since a epifluorescence microscope was used, meaning the resolution of cell contours is not the highest.[97]
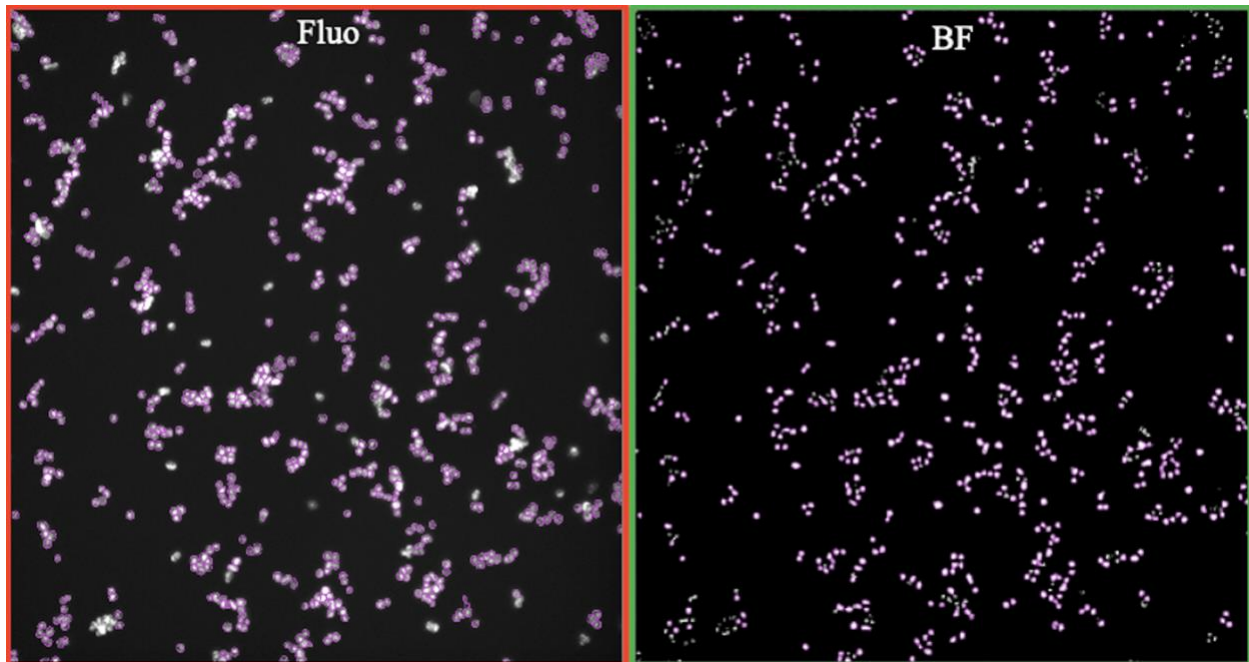
Figure 9. Cell area determination of TOV-112D cells stained with 2 µM of cytoplasmic dye DRAQ9. Fluorescence (fluo) images (red frame) and high-contrast BF images (green frame) were taken of the same field views. The identified cell contours determined from StarDist are shown in magenta. In this example shown, the mean cell area obtained from the fluorescence image was 173.01 µm^2, while the mean cell area obtained from the BF image was 91.12 µm^2.

Thus, the true cell area is somewhere in between the cell areas determined from the fluorescence and BF images. Nonetheless, it was important to quantify how well our high-contrast BF images determine cell areas and led us to question if this underestimation of cell area affects the results of CRRC.

2.5.3 Robustness of CRRC to cell area

We confirmed that our high-contrast BF images underestimate cell area, so we decided to investigate if this underestimation of cell area affects the results of CRRC. Hypothetically, since we are interested in kinetics of fluorescence intensities rather than the actual intensity values, the consistent loss of cell area should not significantly influence the results of CRRC. Nevertheless, we conducted a CRRC experiment of cross-membrane transport in TOV-112D cells and obtained
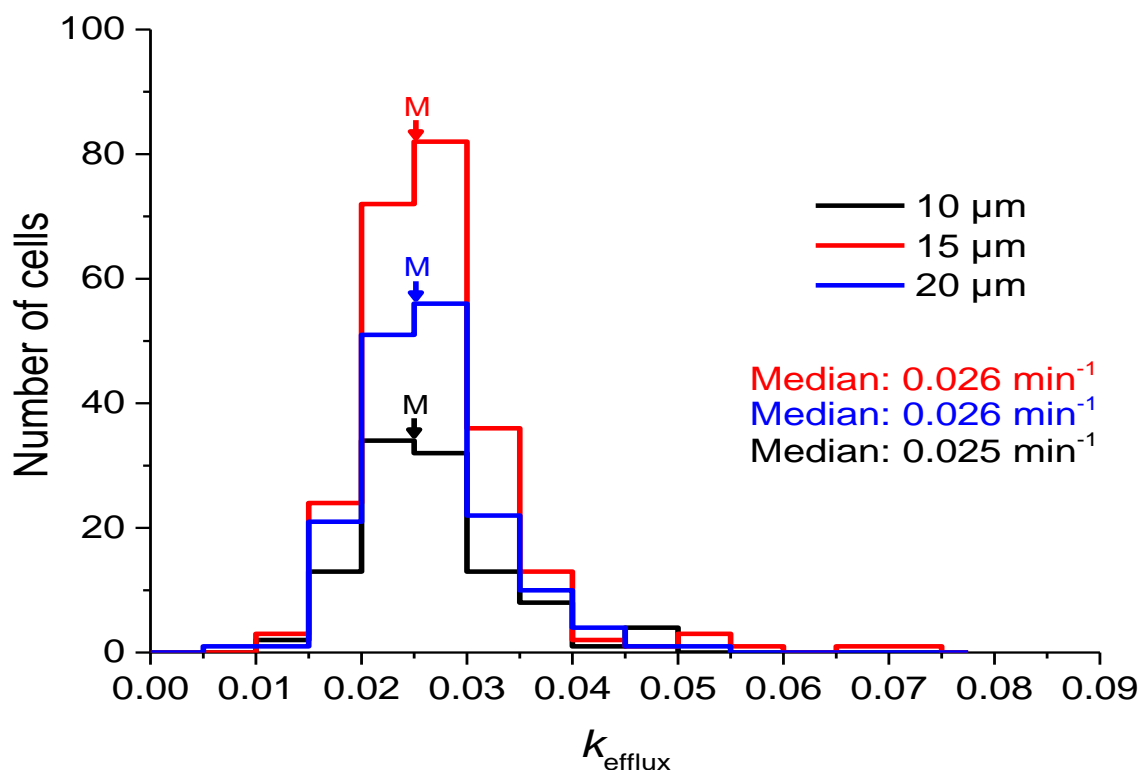
Figure 10. Illustration of CRRC's insensitivity to cell diameters (areas). Kinetic histograms of k_{efflux} rate constants found in TOV-112D cells using 10, 15, and 20 µm estimated cell diameters are displayed. The variation in sample sizes is attributed to differences in cell identification and filtering; however, each distribution comprised of over 100 cells. Median k_{efflux} values are shown and their positions are designated by the arrows. The k_{efflux} rate constant distributions were compared to each other using the two-sample Kolmogorov-Smirnov test and were found not to be significantly different at the 0.05 level. The p values were 0.66 (10 and 15 µm), 0.82 (10 and 20 µm), and 0.81 (15 and 20 µm).

k_{efflux} rate constant distributions using different recognized cell diameters (areas) (**Figure 10**). The cells were analyzed using the Laplacian of Gaussian (LoG) detector in TrackMate. With this detector, cells are recognized based on an estimated diameter that can be varied. The estimated cell diameters were 10, 15, and 20 µm. It was found that the k_{efflux} distributions had nearly identical median k_{efflux} values and were found not to be significantly different, according to the Kolmogorov-Smirnov test at the 0.05 level. Therefore, it is suitable to use our thresholding method for processing of BF images, as the results of CRRC are unaffected by the systematic underestimation of cell areas.

2.5.4 Cell movement during acquisition of matching fluorescence and BF images

Now that we selected to use processed BF images in our new workflow, we were interested in cell motility between matching fluorescence and BF images. Specifically, we wanted to confirm that the cell contours determined in the BF images are applicable to the fluorescence images because of the brief time gap that exists between a fluorescence image and an accompanying BF image. Hence, we assessed the extent of cell motility within this brief time frame. For the purpose of recording cell tracks, we carried out high frequency (1 image per 10 s) time-lapse BF imaging of motile TOV-112D cells (**Figure 11A**). From the cell tracks, we discovered that speed of cell migration did not follow a normal distribution (**Figure 11B**). The median of the distribution was approximately 150 µm/h and the interquartile range was 40 µm/h. The fastest cell moved at speed of $v \approx 401$ µm/h. In a similar study that measured the motility of single cells using an ImageJ plugin, the fastest determined cell speed of MDA-MB-231 (breast cancer) cells was around 70 µm/h.[98] The difference in speeds could be attributed to the time interval of image acquisition — we acquired images every 10 s, while images were taken every 5 min in the other study. With high-frequency image acquisition, we wanted to accurately quantify cell movement for the short

A
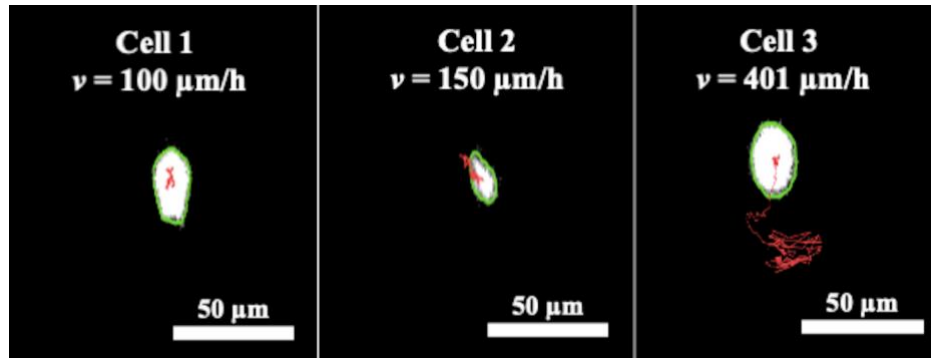
B
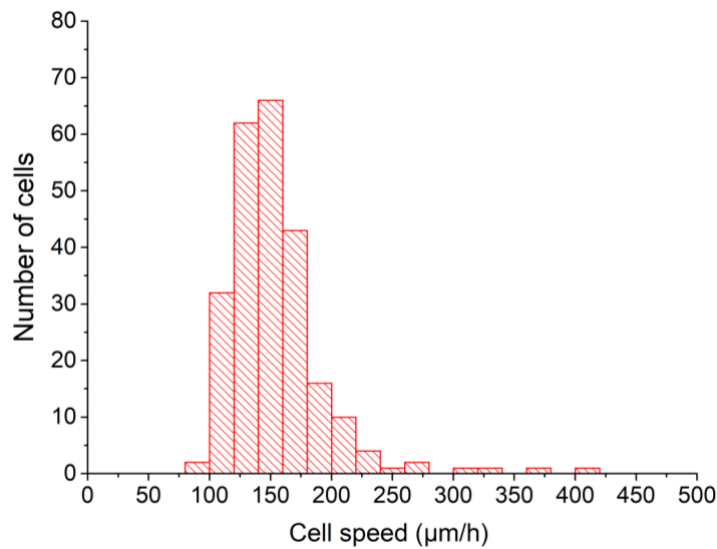
Figure 11. (A) Speed determination of motile TOV-112D cells found from high frequency time-lapse BF imaging (1 image per 10 s). The three panels show cells with varying levels of motility; red lines show representative cell tracks. Cell contours (green) show cell positions at the start of time-lapse imaging. Average speeds for each cell are shown in the panels. **(B)** Distribution of cell movement speeds (µm/h) shown as a histogram. Shapiro-Wilks normality test at the 0.05 level revealed that the distribution was not normal ($P = 2.2 \times 10^{16}$). The interquartile range of the distribution was 40 µm/h, while the distribution's peak was roughly 150 µm/h. The quickest cell moved at a rate of about 401 µm/h.

duration it takes for acquiring matching fluorescence and BF images, which was timed to be approximately $t_1 = 3.0$ s. Hence, the shift of the quickest cell during this short time frame is $x = vt_1 = 0.33$ µm. Further, the mean cell diameter (SD) was $d = 13$ µm (3 µm). The error that such a shift in cell position can cause in intracellular fluorescence intensity integration over the area within the cell contours is of the order of $x/d \approx 0.025$ (**Figure 12**). Accordingly, the error in

31
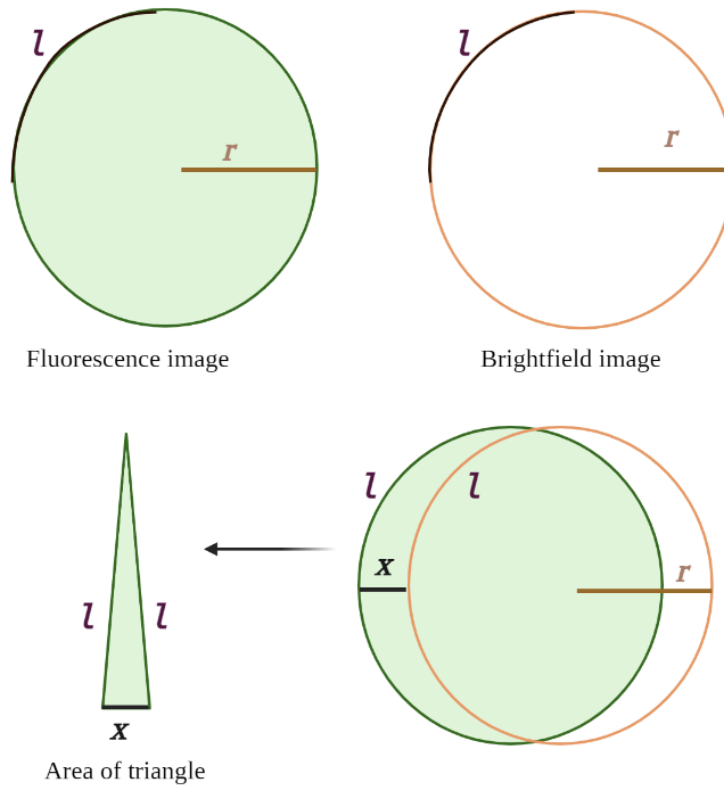
Figure 12. Schematic depiction of the effect of cell movement on fluorescence intensity integration. Let us assume that $x/r \ll 1$, where x is the distance travelled by the cell and r is a cell radius. In this case, the cell area above x can be assumed to be a triangle: $s = xl/2$. The total area that is excluded from fluorescence intensity integration is $S = 2s = 2xl/2 = xl = x(2\pi r/4) = \pi xr/2$ and the area would be integrated is that of a circle: $S_{circle} = \pi r^2$. The area excluded for fluorescence intensity integration is smaller than the area of the circle. Hence, the relative error of cell area determination for integrating fluorescence is $\Delta S = S/S_{circle} = \pi xr/(2\pi r^2) = x/(2r) = x/d$.

intracellular fluorescence intensity caused by the short time gap between the fluorescence image and BF image is roughly 2.5%, which is negligible even for the fastest moving cell. Thus, cell positions in the matching fluorescence and BF images can be assumed to be identical.

2.5.5 Consideration of focusing for fluorescence intensity integration

We continued our investigation in fluorescence intensity integration, but this time considering the effects of focusing. Most modern advanced microscopes have the configuration option of setting distinct Z-positions for different imaging modes, but we wanted to see if our new workflow is applicable for microscopes without this option, so we performed the following

experiment. We stained TOV-112D cells with the cytoplasmic probe DRAQ9. DRAQ9 was chosen as the probe because it did not a require an inhibitor like the cross-membrane transport substrate, fluorescein, and since we used an apochromatic lens (HC PL APO 10×/0.45), DRAQ9 (far red) is roughly on the same focal plane as fluorescein (green). First, a high-contrast BF image was taken and used for cell contour determination. Then, we focused on the cells in the fluorescence mode and took an image for reference. From experience, it is more likely to be out of focus by 5 µm, hence we took out-of-focus fluorescence images 5 µm below and 5 µm above the reference. Intracellular fluorescence intensities were found in all fluorescence images using the
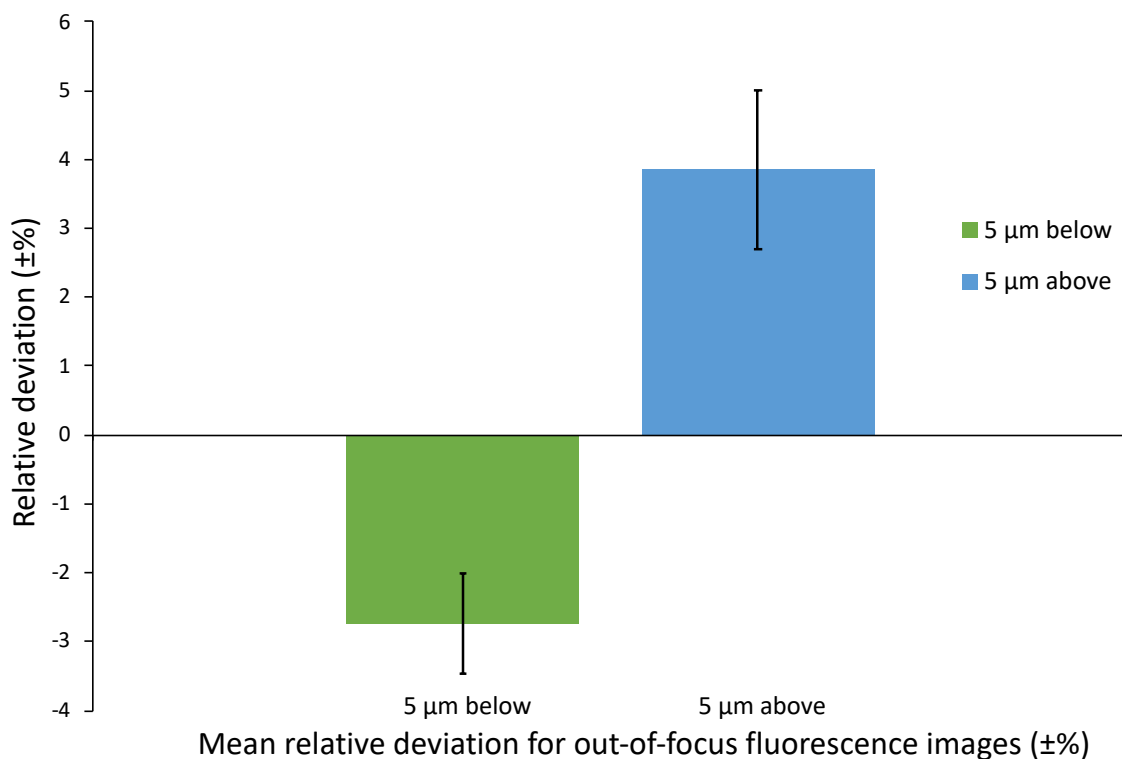
Figure 13. Mean relative deviations with 95% confidence intervals (CI) in fluorescence intensities at different Z positions. TOV-112D cells were stained with 2 µM of the cytoplasmic probe DRAQ9. Cell contours were found from taking a high-contrast BF image. An in-focus fluorescence image was taken for reference and fluorescence images 5 µm below and 5 µm above the reference were taken. Intracellular fluorescence intensities obtained from the in-focus image were used to find relative deviations in intensities for the out-of-focus images. The mean relative deviations were -2.2% (95% CI, -1.46% – -2.94%) for the fluorescence image taken 5 µm below and 3.6% (95% CI, 2.4% – 4.8%) for the fluorescence image taken 5 µm above the reference.

cell contours determined from the high-contrast BF image. Fluorescence intensities for cells in the in-focus image were used as references to find the mean relative deviations in fluorescence intensities for the out-of-focus images, which were 2.2% (95% confidence interval [CI], -1.46% – -2.94%) for 5 µm below and 3.6% (95% CI, 2.4% – 4.8%) for 5 µm above (**Figure 13**).

2.5.6 New CRRC workflow in practice

A comparison of the new and original workflows is schematically depicted in **Figure 14**. To establish the effect of cell motility on the two workflows, we studied cross-membrane transport in motile TOV-112D cells using both workflows and compared their final histograms. For accurate cell tracking in the new workflow, we set the time interval between subsequent BF images (t_2) to be shorter than the time required for the fastest cell (with speed v) to travel a distance equal to the mean cell diameter d: $t_2 << d/v$. Consequently, we used the determined values of $v = 401$ µm/h and

Original workflow

| Acquisition of time-lapse fluorescence images of intracellular substrate (product) |
| Staining cells with propidium iodide and taking a single fluorescence image of intracellular PI |
| Automated determination of cell contours on the propidium iodide fluorescence image only using the Analyze Particles tool in Fiji |
| Determination of fluorescence intensities of the substrate (product) in the time stack of images using cell contours drawn in the propidium iodide image using Fiji |

New workflow

| Acquisition of time-lapse fluorescence images of intracellular substrate (product) accompanied by brightfield images |
| Processing of fluorescence and brightfield images in Fiji |
| Merging pairs of the processed fluorescence and brightfield images into composite images in Fiji |
| Automated (*i*) determination of cell contours, (*ii*) cell tracking, and (*iii*) determination of intracellular fluorescence intensity of the substrate (product) in the time-stack of composite images using TrackMate + StarDist |

| Construction of time dependencies of fluorescence intensities in Excel, exponential fitting of these dependencies to find rate constants in OriginPro, and plotting a kinetic histogram "number of cells vs rate constant" in OriginPro |

Figure 14. Comparison of the original (left) and new (right) workflows. The last step of kinetic analysis remained the same for both workflows.

d = 13 µm from the "Cell movement during acquisition of matching fluorescence and brightfield

images" section, to set t_2 = 1 min. The two workflows were used to acquire their respective time-

lapse images and to construct time dependencies of intracellular fluorescence intensities (kinetic

curves). The kinetic curves were fitted with a single exponential decay function to calculate the

unimolecular rate constant of cross-membrane transport, k_{efflux}.

To examine the effect of cell motility on both workflows, we looked at kinetic curves for

cells with low and high motility. For the high motility cell, we found that the two workflows

produced noticeably different kinetic curves and k_{efflux} values due to the absence of the cell tracking
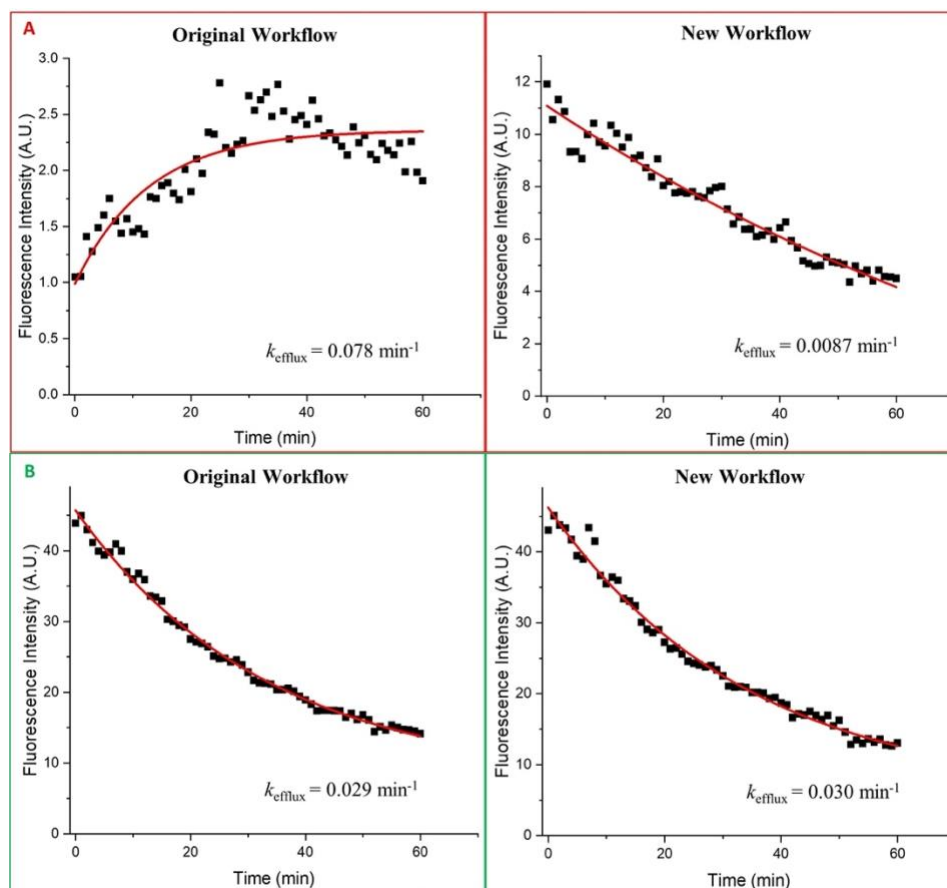
Figure 15. Examples of kinetic curves produced by the original and new workflows. All four kinetic curves were fitted to the single exponential decay function, ExpDec1, available in OriginPro. The black squares represent intracellular fluorescence intensities at specific time points and the exponentially fitted curves are shown in red. (**A**) High-motility cell. The original workflow produced an unusual kinetic curve. OriginPro accepted this curve and generated a k_{efflux} value that is 9-fold greater than the rate constant obtained from the new workflow. (**B**) Low-motility cell. The two workflows recorded similar kinetic curves and k_{efflux} values.

35

in the original workflow leading to abnormal kinetic behaviour (see example in **Figure 15A**). Contrary, the two workflows recorded similar kinetic curves and k_{efflux} values for the low motility cell, as cell tracking was not required to acquire the correct kinetic curve for this particular cell (see example in **Figure 15B**). Hence, the two workflows produced different k_{efflux} values for cells with high motility, as cell tracking is absent in the original workflow.

An in-depth explanation of the abnormal kinetic curve behaviour seen with the original workflow starts with the single cell contour mask used for fluorescence integration. In the original workflow, the contour mask is acquired at the end of the time-lapse experiment., which is likely to differ for highly motile cells whose positions change gradually during the experiment. Additionally, the manual addition of PI used to obtain the cell contour masks, may cause an unintentional, last shift in the cell's position. Accordingly, for a highly motile cell, little to no fluorescence will be integrated in the initial stages of the experiment because the true cell position will be mostly outside of the cell contour mask. However, the location of the cell will gradually overlap with the identified cell contour mask as it moves closer to its final destination leading to an increase in fluorescence over time. This can be seen in **Figure 15A**, as the increase in fluorescence occurs until around 40 minutes. At around 40 minutes is when the cell stops moving, which ended the overlapping process between the true cell position and the cell mask as well as the increase in fluorescence intensity. Then, a sharp decline in fluorescence can be seen after 40 minutes, which appears to be the part of the kinetic curve where OriginPro calculated the relatively high k_{efflux} value from. Hence, the inconsistency between the true cell position and determined cell contour mask is what causes relatively higher k_{efflux} values in the original workflow.

A significant finding from the in-depth comparison of the fluorescence-decay kinetics of cells with varying motility is that the rate constant of highly motile cells was likely overestimated

using the original workflow. When comparing the CRRC histograms produced by the two workflows, a distinguishable shift to the right is seen for the histogram of the original workflow (**Figure 16**). The original workflow produced a median k_{efflux} that was 1.4-fold greater than the median k_{efflux} value of the new workflow. Further, the distribution of original workflow had a 12-fold greater skewness value than the new workflow's distribution, indicating there were more positive k_{efflux} values in the original workflow's distribution. We then investigated if there was a statistically significant difference between the rate constant distributions using the two-sample Kolmogorov-Smirnov test. The distributions in **Figure 16** were shown to differ significantly the 0.001 level ($D = 0.376$, $D_\alpha = 0.209$, $p = 2.82 \times 10^{-11}$). It is noteworthy to mention that the two distributions in **Figure 16** have different sample sizes. This occurs since the two workflows differ
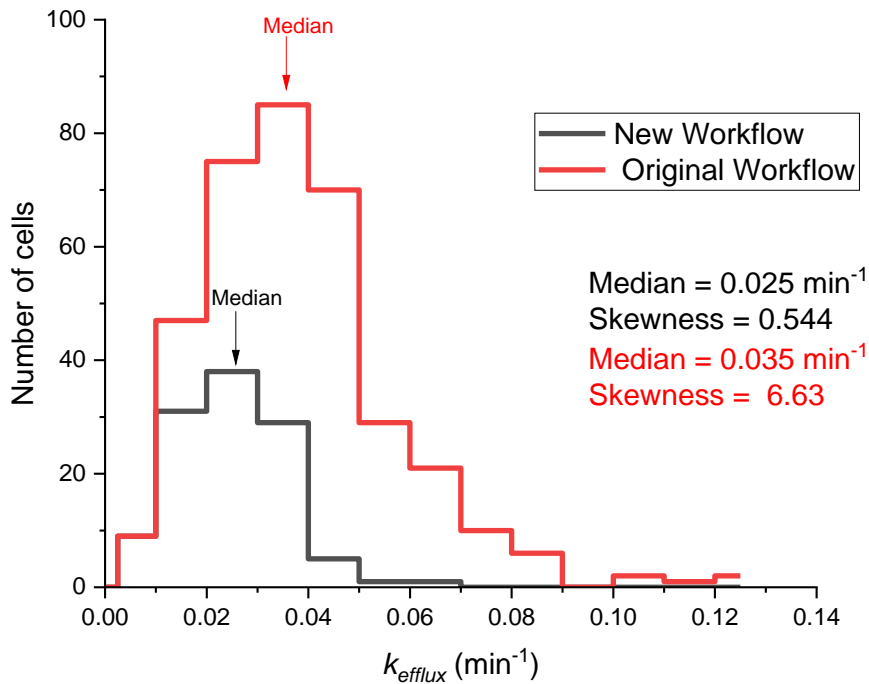
Figure 16. CRRC histograms of cross-membrane transport activity, represented by k_{efflux}, in TOV-112D cells. The variation in sample size is caused by the different cell contour identification processes in the two workflows. Both sample sizes consisted of over 100 cells. Median and skewness values are displayed, with the positions of the median values indicated by the arrows. The histogram acquired from the original workflow is evidently skewed towards the right. The k_{efflux} distributions of the two workflows were found to be statistically different by the two-sample Kolmogorov-Smirnov test at the 0.001 significance level ($p = 2.82 \times 10^{-11}$).

in the cell contour identification step; nonetheless, both sample sizes were greater than a 100 cells (miniumium sample size for statistical signficance) and the Kolmogorov-Smirnov test is insensitive to the difference in sample sizes. Thus, based on these results we can conclude that the new workflow produces a CRRC histogram that is robust to cell motility, while the original workflow produces a positively skewed histogram caused by the absence of cell tracking.

2.6 Conclusion

The development of the new workflow is a significant move towards CRRC becoming a practical analytical tool. A wider range of cell types, which include motile cells, can now be reliably analyzed by CRRC. Consequently, this workflow will allow us to initiate CRRC studies of reactions other than cross-membrane transport. In recent years, significant advancement has been made in the design of high-quality fluorogenic substrates for intracellular enzymes. Specifically, such substrates have been made for a significant xenobiotic-metabolizing enzyme linked to chemoresistance: aldehyde dehydrogenase,[99,100] and cytochrome P450.[101] We predict that using the new CRRC workflow along with these substrates will facilitate the discovery of novel predictive biomarkers of chemoresistance.[19]

Chapter Three
APPLYING NEW CYTOMETRY OF REACTION RATE CONSTANT (CRRC) WORKFLOW TO AN INTRACELLULAR ENZYME: CYTOCHROME P450

3.1 Background

With the development of the new workflow, our aim was to study chemoresistance mechanisms that have yet to be analyzed by CRRC: DNA damage repair and drug metabolism. For DNA damage repair, we are interested in analyzing the activity of enzyme by the name of ERRC1, since this enzyme has been heavily linked to chemoresistance.[102] Unfortunately, a fluorogenic substrate has not yet been developed for ERCC1, so we chose to focus on drug metabolism instead.

3.1.1 Introduction to cytochrome p450

For drug metabolism, one of the major enzymes involved in this mechanism is cytochrome p450 (CYP) as this superfamily of enzymes are responsible for ~75% of total drug metabolism.[103] CYPs are located in the inner membrane of the mitochondria or the endoplasmic reticulum of cells in several tissues, for example, in the liver, kidney, lung, small intestine, brain, and heart.[104] The human CYP superfamily is composed of approximately 60 genes and is divided into 18 families and 44 subfamilies. Members of the same family share at least 40% amino acid identity and members of the same subfamily share at least 55% amino acid identity.[105] Their nomenclature is composed of the CYP root, indicating the cytochrome P450 superfamily; followed by a Arabic numeral, indicating the family (*e.g.*, CYP1, CYP2, CYP3); then a capital letter, which indicates the subfamily (*e.g.*, CYP1A, CYP2B, CYP3A); and another numeral for each member (*e.g.*, CYP1A1, CYP2B6, CYP3A4) [106]. Since CYPs are major players in drug metabolism, they are

linked to chemoresistance in many different types of cancer such as lung, prostate, breast, and ovarian cancer.[107]

3.1.2 CYP's involvement in chemoresistance

CYPs are hemoproteins — with a single iron protoporphyrin IX prosthetic heme group — that catalyze the hydroxylation of exogenous and endogenous compounds with multiple chemical structures. Furthermore, they are oxidoreductases, *i.e.,* they activate molecular oxygen (O_2) at the iron center and incorporate one of the oxygen atoms into an array of substrates.[108] For their reactions, CYPs need the NADPH co-factor as the electron donor and the enzyme cytochrome P450 reductase as the electron transfer partner.[109] A typical CYP-catalyzed hydroxylation is summarized below, with R–H representing a substrate:[110]

$$R\text{–}H + O_2 + NADPH + H^+ \rightarrow R\text{–}OH + H_2O + NADP^+ \tag{3}$$

This reaction deactivates a substrate by converting it to a more polar product, R-OH, which leads to easier elimination of the substrate from the cell. If the substrate is, for example, a chemotherapeutic, the insertion of the hydroxyl group will make the drug lose its anticancer activity and promote its extrusion from the cell. This is how CYPs contribute to chemoresistance, as drug-resistant cells with elevated CYP activity, would have an insufficient chemotherapeutic concentration in their interior.[111]

3.1.3 Analyzing CYP activity by CRRC

Evaluation of CYP activity by CRRC is conceptually more complex than CRRC analysis of cross-membrane transport because of two reasons: location of the catalyst and type of probe that is used in the analysis. While transporters are in the cell membrane, CYPs are intracellular enzymes, found in the inner membrane of the endoplasmic reticulum or the mitochondria. As for the probe, a fluorophore is used as the substrate for cross-membrane transport, because it is simply

extruded out from the interior of cells. Hence, no chemical transformation of the substrate is required. On the other hand, CYPs require a fluorogenic substrate; thus, a fluorescence increase is seen over time in the CYP CRRC assay. To help visualize CRRC analysis of an enzymatic reaction like CYP, an altered schematic representation of the CRRC steps is shown in **Figure 17.** There are a numerous fluorogenic substrates of CYP that could be used for CRRC such as O-alkyl derivatives of resorufin, fluorescein, and coumarin.[112] For this study, we chose pentoxyresorufin, $C_{17}H_{17}NO_3$, a probe that is selective for the CYP2B subfamily,[113,114] because it was commercially available and used in previous CYP activity studies.[115,116]
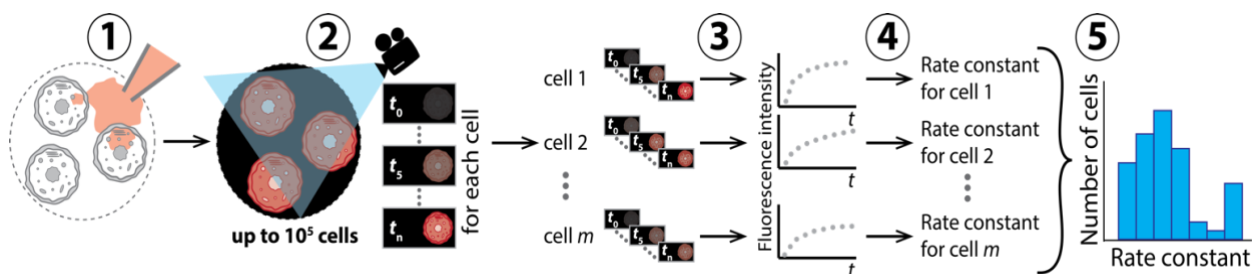
Figure 17. A schematic illustration of the steps involved in CRRC analysis of an enzymatic reaction. The two differences from CRRC analysis of cross-membrane transport are: 1) a fluorogenic substrate is used instead of a fluorescent one and 2) intracellular fluorescence increases are monitored instead of fluorescence decreases.

3.1.4 Enzyme kinetics relevant to CRRC of intracellular enzymatic reactions

It is important discuss the kinetics that underly CRRC analysis of enzymatic reaction. CRRC is best suited for cellular reactions that proceed through the formation of intermediate complex. Enzymatic reactions, such as CYP-mediated drug metabolism, meet this criterion as these reactions proceed through an intermediate enzyme-substrate complex. A typical enzymatic reaction is shown below:[117]

$$E + S \leftrightarrow ES \rightarrow E + P \tag{4}$$

where E is an enzyme, S is a substrate, ES is the intermediate enzyme-substrate complex, and P is the product.

Furthermore, the rate of product formation in this reaction is given by the Michaelis-Mentens equation, as presented below:[118]

$$\frac{d[P]}{dt} = \frac{V_{max}[S]}{K_M + [S]} \tag{5}$$

where V_{max} is the maximum reaction velocity and K_M is the Michaelis constant.

CRRC evaluates an enzymatic process by determining the ratio between V_{max}/K_M, which is equivalent to the pseudo-first order rate constant, k. Note that the rate constant is a robust parameter that is uninfluenced by changes in experimental settings. Here, we measured the pseudo-first order rate constant, k_{CYP}, which characterizes CYP activity in a single cell. Measuring the first-order rate constant requires that first-order conditions are satisfied, so the substrate concentration must be lower than K_M. If substrate concentration is greater than K_M, product concentration would depend linearly on time, so the kinetic trace would fail exponential fitting. If a cell produces a kinetic trace that fails exponential fitting, it would not be included in the histogram. Therefore, we take into consideration fundamental enzyme kinetics principles to ensure that we obtain reliable data.

Moreover, it is worth mentioning that finding the ratio between V_{max}/K_M to calculate the rate constant does not rely on knowing the intracellular substrate concentration. The reason to avoid dependence on intracellular substrate concentration is due to impracticality. Intracellular substrate concentration cannot be controlled in the activity analysis of an intracellular enzyme like CYP. Furthermore, this type of analysis requires the use of a fluorogenic substrate that is initially nonfluorescent, so it would be difficult to determine its exact concentration in cells. Hence,

measuring the first-order rate constant is the most pragmatic method for evaluating intracellular enzyme activity.

3.2 Experimental layout

The goal of this work was to assess the applicability of the new CRRC workflow for analyzing the activity of a drug-degradation pathway catalyzed by cytochrome P450 (CYP), a primary group of enzymes metabolizing chemotherapeutics. We tested a fluorogenic substrate suitable for interrogating intracellular activity of CYP and developed an experimental protocol that considers the interferences of other reactions. It was found that the substrate and experimental protocol is suitable to analyze CYP activity, as intracellular fluorescence increase was seen and maintained over time. We then tested intraplate variability (repeatability) of CRRC analysis of CYP activity. Unexpectedly, we obtained statistically different k_{CYP} distributions of the same cell line split into separate culture plates that were analyzed under the same conditions. This led us to test intraplate variability of CYP activity and we found that one region of the cell culture plate had cells with significantly different CYP activity than other regions.

3.3 Materials and methods

3.3.1 Cell culture

HCT-116 colon cancer cells were purchased from ATCC and grown in McCoy's 5A modified medium (Gibco, Grand Island, NY, USA, Cat. No: 16600082) supplemented with 10% fetal bovine serum (Gibco, Grand Island, NY, USA, Cat. No: 12483-020). Cells were cultured in 60 mm plastic-bottom dishes (Sarstedt AG&Co, Numbrecht, Germany, Cat. No: 83.3901) and 35 mm plastic-bottom dishes (Nest Biotechnology Co, Wuxi, Jiangsu, China, Cat. No: 706001) for imaging. Cells were cultured in an incubator at 37°C with a humidified 5% CO_2 atmosphere until they reached 70% confluency.

3.3.2 CRRC experimental protocol for CYP activity analysis

To assess CYP activity, we followed O-dealkylation of pentoxyresorufin (a fluorogenic CYP substrate) forming resorufin (a fluorescent product) over time. Pentoxyresorufin is a lipophilic substrate, thus it was diluted in DMSO. Probenecid (1 mM), an organic anion transporter inhibitor, was added to prevent extrusion of the product and dicoumarol (25 μM), an inhibitor of the enzyme NAD(P)H Quinone Dehydrogenase 1, was added to inhibit unwanted transformation of the product (resorufin) into non-fluorescent dihydroresorufin. The full CRRC CYP activity analysis protocol involved the following four steps. First, we removed the cell culture medium and washed cells once with 1 mL of PBS (Cytiva, Logan, Utah, USA, Cat. No: SH30256.01). Second, we added 1.2 mL of HBSS solution containing 1 mM probenecid and 25 μM dicumarol to the cell culture plate. Third, we started started image acquisition with alternating fluorescence and BF modes every 30 seconds for 1 hour. Fourth, after 3 minutes, we removed 0.6 mL of the solution in the cell culture plate and replaced it with 0.6 ml of HBSS solution containing 15 μM pentoxyresorufin and let image acquisition continue until the end of the experiment.

3.3.3 Image acquisition

The same microscope, objective lens, camera, and microscope capabilities were used as the previous chapter "Developing a New Workflow for Cytometry of Reaction Rate Constant that Addresses Cell Motility". Note that a RHOD cube was used to detect the fluorescence of resorufin.

3.3.4 Image settings

The following are the image settings for each Figure. For **Figures 20, 21, and 22**, BF: 4×4 binning, 7.81 ms exposure, high well capacity, intensity 14, aperture 12, Tl-Fld 46, 229–234

intensity threshold. Fluorescence: RHOD channel, 4×4 binning, 200 ms exposure, low noise, FIM: 30%, Il-Fld 6.

3.3.5 Image processing in Fiji

We followed the same image processing procedure discussed in the previous chapter, "Developing a New Workflow for Cytometry of Reaction Rate Constant that Addresses Cell Motility" with no changes made.

3.3.6 Formation and analysis of kinetic traces

The kinetic analysis was the same as previous chapter, "Developing a New Workflow for Cytometry of Reaction Rate Constant that Addresses Cell Motility" except for one change. Here, the kinetic traces were exponentially fitted with the "ExpAssocDelay1" function in OriginPro for calculation of the rate constant, k_{CYP}. The "ExpAssocDelay1" function is shown below:

$$y = Yb + A(1 - e^{-\frac{(x-TD)}{Tau}})$$
(6)

where Yb = baseline, A = amplitude, TD = time offset, Tau = time constant, and k_{CYP} is a

derived parameter = $1/Tau$

3.3.7 Cell population analysis

No changes were made from the preceding chapter, "Developing a New Workflow for Cytometry of Reaction Rate Constant that Addresses Cell Motility" except for the consideration of another descriptive statistic measure, interquartile range (peak width).

3.4 Results and discussion

3.4.1 Validation of CYP CRRC experimental protocol

As a CRRC study of CYP activity was never done before, it was of primary focus to develop and validate a protocol for this purpose. As mentioned before, pentoxyresorufin was

selected as the fluorogenic substrate to interrogate CYP activity. CYP catalyzes the O-dealkylation of pentoxyresorufin to form the fluorescent product, resorufin. This reaction will cause intracellular fluorescence to increase over time. However, other side reactions could affect fluorescence accumulation over time. Resorufin could be extruded out of the cell or undergo conversion into a non-fluorescent product. Hence, we identified two inhibitors to prevent these unwanted processes from occurring: probenecid and dicumarol. Probenecid is an organic anion
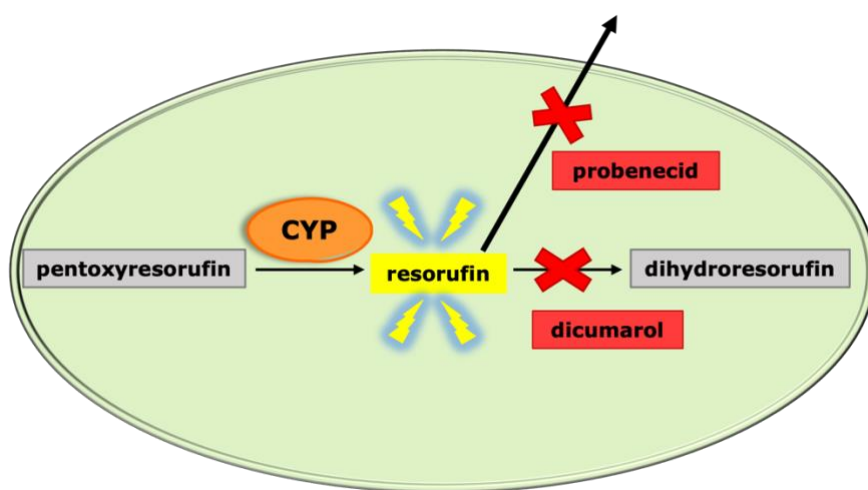
Figure 18. Schematic illustration of CYP activity analysis by CRRC. The initially non-fluorescent CYP substrate pentoxyresorufin (grey) is converted into fluorescent product resorufin (yellow) by CYP enzymes. CYP enzymatic activity in single cells is quantified by the accumulation of resorufin fluorescence intensity. Dicumarol (red), an inhibitor of the enzyme NAD(P)H Quinone Dehydrogenase 1, is added to avoid further transformation of resorufin into dihydroresorufin (grey), which is non-fluorescent. Probenecid (red), an inhibitor of organic anion transport, is added to avoid leakage of resorufin out of the cell.

transporter inhibitor that prevents expulsion of resorufin and dicoumarol is an inhibitor that prevents the transformation of fluorescent resorufin into non-fluorescent dihydroresorufin. A schematic depiction of the CRRC CYP assay is shown in **Figure 18**.

Now that an experimental protocol has been developed, we wanted to test the new CRRC workflow for CYP activity analysis. An example set of matching high-contrast BF and fluorescence images is shown in **Figure 19**. To reiterate a point made in the preceding chapter
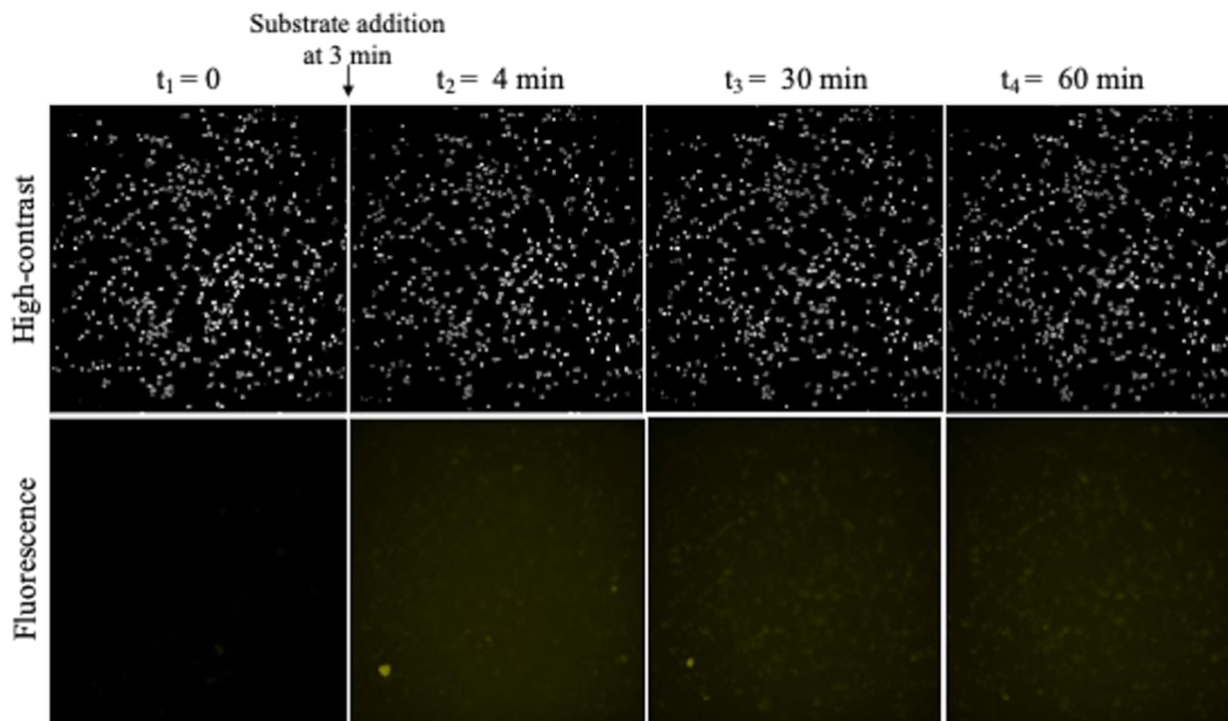
Figure 19. Example set of images obtained with the new CRRC workflow for CYP activity analysis. High-contrast BF images (top) are accompanied by fluorescence images (bottom) taken every 30 seconds for 1 hour. Images taken at 0, 4, 40 and 60 min are shown. Fluorogenic substrate, 15 μM pentoxyresorufin, was added after 3 minutes. Fluorescence images are displaying intracellular accumulation of the fluorescent product, resorufin. Resorufin fluorescence emission was detected by the RHOD cube. Additionally, 1 mM probenecid and 25 μM dicumarol are present in the cell culture plate.

against the use of only fluorescence imaging of substrate conversion, note that no fluorescence is observed at the start of the experiment since no substrate is present. Thus, it would nearly be impossible to locate cells using fluorescence images before substrate addition; however, the matching high-contrast BF image allows for cell contours to be identified in the pre-substrate addition stage of the experiment. Once the substrate is added to the cell culture plate after the 3-minute mark, an immediate increase in fluorescence can be seen. From these images, it appears that the CRRC experimental procedure for interrogating CYP activity with the new workflow is practical.

To ensure that the CRRC protocol for CYP activity analysis is functional with the new workflow, we performed a trial run of the experiment in HCT-116 cells to analyze intracellular

fluorescence. After we obtained the intracellular fluorescence intensities, we averaged the intensities at each time point to generate a representative kinetic trace of CYP activity (**Figure 20**). A drastic increase in intracellular fluorescence is observed after substrate addition at 3 minutes. Further, it appears that intracellular fluorescence is sustained for the entirety of the experiment, indicating the two inhibitors, probenecid and dicumarol, are indeed promoting the
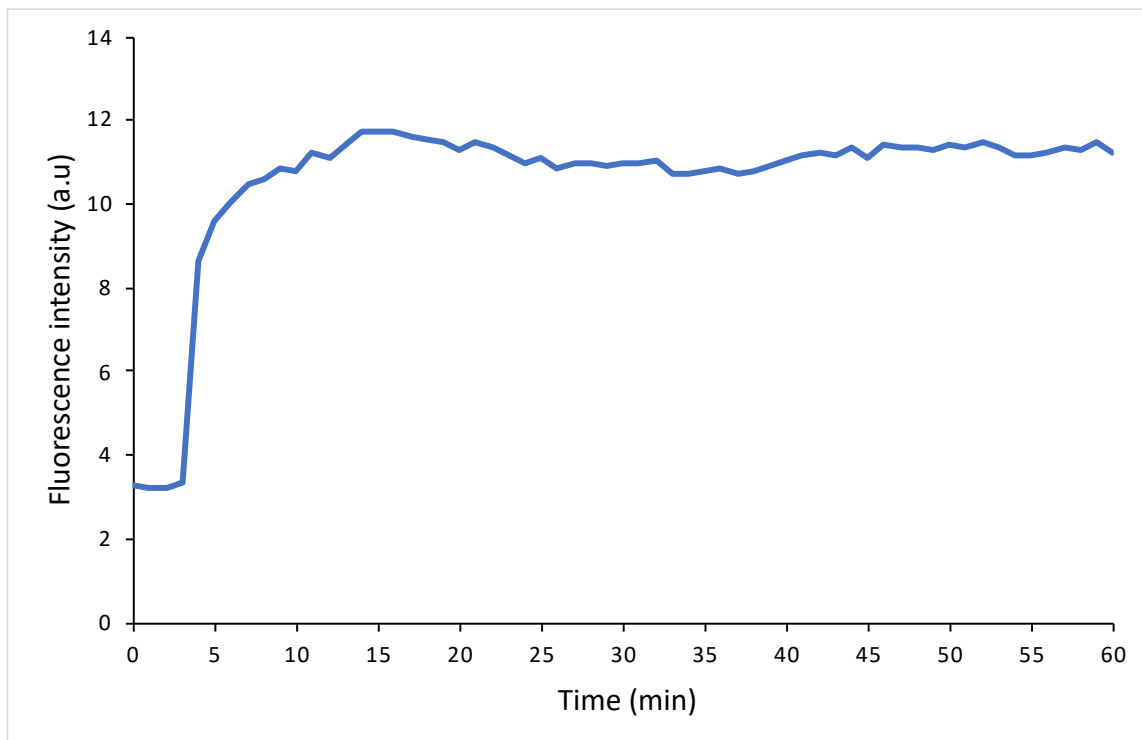
Figure 20. Population kinetic trace of CYP activity in HCT-116 cells. A sharp increase in intracellular fluorescence can be seen after substrate addition at 3 minutes. Fluorescence is maintained for the duration of the experiment.

accumulation of the fluorescent product. Hence, it appears that the CRRC protocol for interrogating CYP activity is successful with the new workflow and can be used for further experiments.

3.4.2 Interplate variability of CYP CRRC assay

After showing the apparent success of studying CYP activity using the new CRRC workflow, the next goal was to prove the repeatability of the assay. To prove repeatability, the CYP CRRC

assay was performed with HCT-116 cells split into two cell culture plates analyzed under the same

conditions. It was predicted that k_{CYP} distributions originating from these two plates should

produce similar histograms due to the fact that the same cells were analyzed under the same

conditions. CRRC histograms of CYP activity for the two plates of HCT 116 cells are shown in

Figure 21, with the first plate of cells representing "trial 1", and the second plate of cells

representing "trial 2". From observing the histograms, they are clearly not superimposable as

expected. To understand the difference in the appearance of the histograms, the descriptive

statistics of the k_{CYP} distributions from each trial were investigated. The descriptive statistics

(median k_{CYP}, interquartile range, and skewness) for each distribution are shown in **Table 1**.

Despite the difference in appearance of the histograms, both trials had the exact same median k_{CYP}
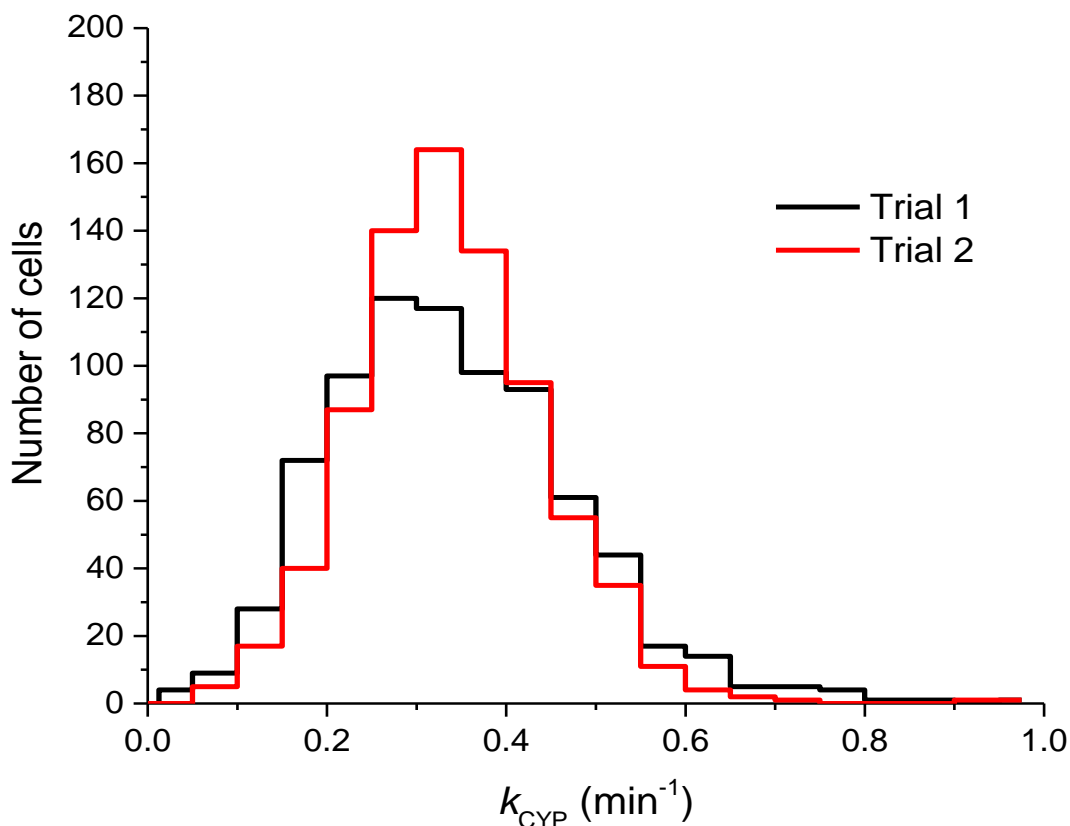
Figure 21. CRRC histograms for repeated trials of CYP CRRC activity analysis in HCT 116 cells.
Approximately 800 cells were analyzed in each trial. The k_{CYP} distributions of the two trials were found to
be statistically different by the two-sample Kolmogorov-Smirnov test at the 0.05 significance level
($p = 0.0034$).

values. However, the difference in distributions could be attributed to the variation in interquartile range, as the variation in skewness was only 5.5%. The variation between interquartile range for the trial distributions was 31.6%, with trial 2 having a larger interquartile range (larger peak width), which can be seen in the histogram. For some reason, there was more spread of the data points in the middle portion of the trial 2's distribution. Moreover, the two-sample Kolmogorov-Smirnov test confirmed that the distributions in **Figure 21** were significantly differently at the 0.05 level ($D = 0.088$, $D_\alpha = 0.068$, $p = 0.0034$). Hence, we unexpectedly found that k_{CYP} distributions of repeat trials were significantly different, likely caused by their difference in interquartile range.

Table 1. Descriptive statistics of k_{CYP} distributions for repeated trials of CRRC CYP activity analysis in HCT-116 cells. The median k_{CYP}, skewness, and interquartile range are shown for each trial. The variation (%) of each parameter is shown between trials.

Parameter	Trial 1	Trial 2	Variation
Median k_{CYP}	0.33 min^{-1}	0.33 min^{-1}	0
Interquartile Range	0.13 min^{-1}	0.19 min^{-1}	31.6%
Skewness	11.27	10.65	5.5%

3.4.3 Intraplate variability of CYP CRRC assay

The difference in k_{CYP} distributions of repeat trials led us to investigate the variability within the same cell culture plate. We performed the CYP CRRC assay for HCT-116 cells and then compared the k_{CYP} distributions originating from adjacent regions (positions) of the cell culture plate. Again, we expected that the histograms from each position will appear similar, since the same cells from nearby regions of the cell culture plate were analyzed under the same conditions. CRRC histograms of CYP activity in HCT-116 cells from adjacent regions of the cell culture plate are displayed in **Figure 22.** The histograms for the different regions do not completely overlap, thus suggesting a difference in the distributions. For detailed analysis of the distributions, the
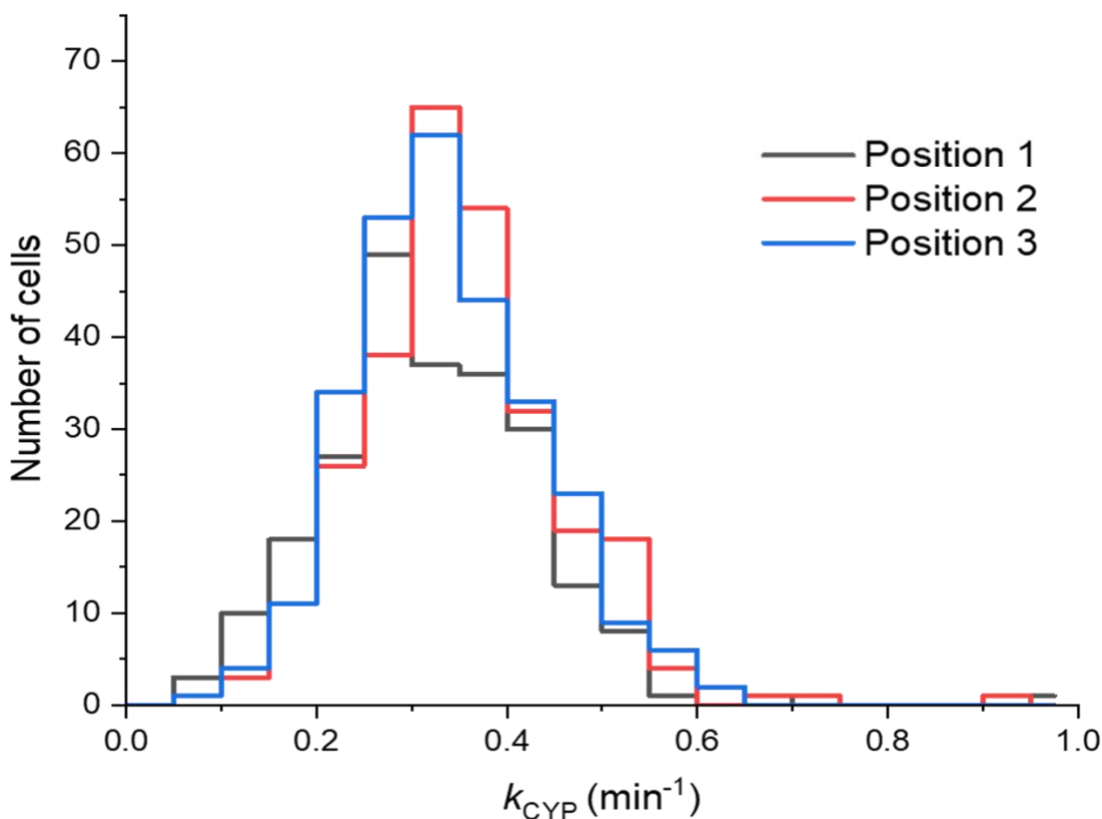
Figure 22. CRRC histograms of CYP activity in HCT-116 cells from different regions within the same cell culture plate. Positions are regions of the cell culture plate that were imaged right next to each other. Over 100 cells were analyzed in each position. Only the distributions of positions 1 and 2 were statistically different from each other determined by the two-sample Kolmogorov-Smirnov test at the 0.05 significance level ($p = 9.25 \times 10^{-4}$).

descriptive statistics (median k_{CYP}, interquartile range, and skewness) are shown in **Table 2**. The parameter that varied the least across the regions was the median k_{CYP} (8.8%), followed by the interquartile range (14.3%). However, the skewness had an extremely high variation of 93.8%, due to the fact that the distribution of position 2 was nowhere near as positively skewed as the other two positions. This is likely the reason for position 2's distribution being significantly different from position 1 according to the Kolmogorov-Smirnov test at the 0.05 level ($D = 0.17$, $D_\alpha = 0.12$, $p = 9.25 \times 10^{-4}$). The distributions of position 1 and 3 were not significantly different ($D = 0.088$, $D_\alpha = 0.11$, $p = 0.13$), and distributions of position 2 and 3 were not significantly different ($D = 0.11$, $D_\alpha = 0.12$, $p = 0.064$). Based on these unanticipated results, there was considerable intraplate variability found, likely caused by the distribution of one region of the cell

culture plate not being as positively skewed as the other regions.

Table 2. Descriptive statistics of k_{CYP} distributions originating from HCT-116 cells found in different regions (positions) of the same cell culture plate. The median k_{CYP}, skewness, and interquartile range are shown for each position. The variation of each measure for all three positions is shown as percentages.

Parameter	Position 1	Position 2	Position 3	Variation
Median k_{CYP}	0.31 min^{-1}	0.34 min^{-1}	0.33 min^{-1}	8.8%
Interquartile Range	0.14 min^{-1}	0.12 min^{-1}	0.12 min^{-1}	14.3%
Skewness	10.00	0.73	11.80	93.8%

3.5 Conclusion

Here, we have shown preliminary progress on the investigation of the activity of an intracellular xenobiotic-metabolizing enzyme, CYP, that has yet to be studied by CRRC, using the newly developed workflow. We found the appropriate fluorogenic substrate and inhibitors to accomplish this assay, confirmed by the increase and maintenance of intracellular fluorescence over time. Then, we tested intraplate variability (repeatability) of CRRC analysis of CYP activity and we unexpectedly obtained statistically different k_{CYP} distributions. This led us to test intraplate variability of CYP activity and we obtained another unanticipated result as the k_{CYP} distribution of one region of the cell culture was significantly different from the rest.

LIMITATIONS

Although the development of a new CRRC workflow that addresses cell motility was a positive step in the right direction, there are several improvements that could be made. First, the thresholding of brightfield images needs to be maintained over the course of the time-lapse experiment. Currently, any slight changes in the Z-position of cells could cause them to be lost from view due to the limited pixel intensity range that is set at the start of the experiment that cannot be adjusted. Fixed thresholding was sometimes responsible for less than desired sample sizes as cells could not be tracked until the end of the experiment, although all histograms shown in this work consisted of population sizes that are statistically significant (over 100 cells). Nonetheless, stronger conclusions can be made with more cells analyzed and included in the CRRC histogram. Increasing the sample size of CRRC will allow it to compete with flow cytometry, in terms of statistical power, as flow cytometry is capable of analyzing thousands of cells. Moreover, another limitation present in the new CRRC workflow is the lack of automation of mechanical operation. Currently, medium exchange occurs through manual operation of a pipette. One problem that arises with manual medium exchange is that unintended disturbances of the cell culture plate may occur and that could cause drastic changes in cell positions leading to unsuccessful cell tracking. Another issue with manual medium exchange is that it takes critical time away that could be used to shorten the time interval to acquire intracellular fluorescence intensities at more time points or it can be used to acquire more imaging positions that will lead to increased sample size. Therefore, addressing these limitations will further improve CRRC and push forward its development as an analytical method

Furthermore, there were some limitations regarding the study of CYP activity using the new CRRC workflow. Even though intracellular fluorescence increase was seen with the

substrate used, it still required a relatively high exposure time (200 ms) and 4×4 binning for its fluorescent product to be detected, which is unideal. Having a shorter exposure time can reduce the time interval and acquiring images without binning will allow for more accurate identification of the cell contours since binning pixelates the cell contours. Additionally, the unanticipated intraplate and interplate variability results found with the CYP activity assay needs to be confirmed that they were uninfluenced by the new CRRC workflow and that cells truly displayed this activity. Nonetheless, good preliminary progress was made with interrogating the activity of an intracellular enzyme never studied before by CRRC.

CONCLUSION AND FUTURE WORK

In this work, we reported on the creation of a new CRRC workflow that represents a significant step forward in the development of CRRC as a practical analytical method. CRRC is now insensitive to cell motility and can now reliably study a wider range of cell types. Because of this new workflow, we began to investigate a critical chemoresistance mechanism that was never studied before by CRRC — xenobiotic metabolism catalyzed by CYP. Furthermore, we exhibited preliminary progress by validating the CRRC protocol for studying this enzyme's activity. We found unexpected intraplate and interplate variability results when studying CYP activity, with more work needed be done to confirm these results. Altogether, CRRC is a cytometry technique that has great promise in the future to be a reliable analytical method used for validation of chemoresistance predictors.

The first next step involves confirming the intraplate and interplate variability results by using the new CRRC workflow on photobleaching of fluorescent beads. Similar rate constant distributions should be obtained from the beads using the new workflow, thereby confirming previous results. After that, proving robustness (*e.g.*, substrate concentration, duration of experiment) and accuracy (*e.g.*, differentiating a high and low CYP activity cell lines) of the CYP CRRC assay will be accomplished. Moreover, there are plans to automate and streamline our kinetic analysis using Python as it is still a laborious process that involves two software: Excel and OriginPro.

REFERENCES

1.   Chabner BA, Roberts TG. Timeline: Chemotherapy and the war on cancer. *Nat Rev Cancer*. 01 2005;5(1):65-72. doi:10.1038/nrc1529

2.   Pérez-Herrero E, Fernández-Medarde A. Advanced targeted therapies in cancer: Drug nanocarriers, the future of chemotherapy. *Eur J Pharm Biopharm*. Jun 2015;93:52-79. doi:10.1016/j.ejpb.2015.03.018

3.   Kummar S, Gutierrez M, Doroshow JH, Murgo AJ. Drug development in oncology: classical cytotoxics and molecularly targeted agents. *Br J Clin Pharmacol*. Jul 2006;62(1):15-26. doi:10.1111/j.1365-2125.2006.02713.x

4.   Zhao J. Cancer stem cells and chemoresistance: The smartest survives the raid. *Pharmacol Ther*. Apr 2016;160:145-58. doi:10.1016/j.pharmthera.2016.02.008

5.   Luqmani YA. Mechanisms of drug resistance in cancer chemotherapy. *Med Princ Pract*. 2005;14 Suppl 1:35-48. doi:10.1159/000086183

6.   Wang X, Zhang H, Chen X. Drug resistance and combating drug resistance in cancer. *Cancer Drug Resist*. 2019;2:141-160. doi:10.20517/cdr.2019.10

7.   Castells M, Thibault B, Delord JP, Couderc B. Implication of tumor microenvironment in chemoresistance: tumor-associated stromal cells protect tumor cells from cell death. *Int J Mol Sci*. 2012;13(8):9545-71. doi:10.3390/ijms13089545

8.   Brunt EM, Paradis V, Sempoux C, Theise ND. Biphenotypic (hepatobiliary) primary liver carcinomas: the work in progress. *Hepat Oncol*. Jul 2015;2(3):255-273. doi:10.2217/hep.15.8

9.   Rueff J, Rodrigues AS. Cancer Drug Resistance: A Brief Overview from a Genetic Viewpoint. *Methods Mol Biol*. 2016;1395:1-18. doi:10.1007/978-1-4939-3347-1_1

10.   Padma VV. An overview of targeted cancer therapy. *Biomedicine (Taipei)*. Nov 2015;5(4):19. doi:10.7603/s40681-015-0019-4

11.   Brace C. Thermal tumor ablation in clinical use. *IEEE Pulse*. 2011 Sep-Oct 2011;2(5):28-38. doi:10.1109/MPUL.2011.942603

12.   Theodorescu D. Cancer cryotherapy: evolution and biology. *Rev Urol*. 2004;6 Suppl 4:S9-S19.

13.   Witzig TE, Gupta M. Signal transduction inhibitor therapy for lymphoma. *Hematology Am Soc Hematol Educ Program*. 2010;2010:265-70. doi:10.1182/asheducation-2010.1.265

14.   Abdulkareem IH, Zurmi IB. Review of hormonal treatment of breast cancer. *Niger J Clin Pract*. 2012 Jan-Mar 2012;15(1):9-14. doi:10.4103/1119-3077.94088

15.   Lassen UN, Makaroff LE, Stenzinger A, et al. Precision oncology: a clinical and patient perspective. *Future Oncol*. Oct 2021;17(30):3995-4009. doi:10.2217/fon-2021-0688

16.   Shepherd FA. Alternatives to chemotherapy and radiotherapy in the treatment of small cell lung cancer. *Semin Oncol*. Apr 2001;28(2 Suppl 4):30-7.

17.   Brasseur K, Gévry N, Asselin E. Chemoresistance and targeted therapies in ovarian and endometrial cancers. *Oncotarget*. Jan 17 2017;8(3):4008-4042. doi:10.18632/oncotarget.14021

18.   Hirakawa A, Sudo K, Yonemori K, et al. A Comparative Study of Longitudinal Toxicities of Cytotoxic Drugs, Molecularly Targeted Agents, Immunomodulatory Drugs, and Cancer Vaccines. *Clin Pharmacol Ther*. 10 2019;106(4):803-809. doi:10.1002/cpt.1442

19.   Bleker de Oliveira M, Koshkin V, Liu G, Krylov SN. Analytical Challenges in Development of Chemoresistance Predictors for Precision Oncology. *Anal Chem*. 09 2020;92(18):12101-12110. doi:10.1021/acs.analchem.0c02644

20.   Krzyszczyk P, Acevedo A, Davidoff EJ, et al. The growing role of precision and personalized medicine for cancer treatment. *Technology (Singap World Sci)*. 2018 Sep-Dec 2018;6(3-4):79-100. doi:10.1142/S2339547818300020

21.   Pritzker KP. Predictive and prognostic cancer biomarkers revisited. *Expert Rev Mol Diagn*. 2015;15(8):971-4. doi:10.1586/14737159.2015.1063421

22.   Bonneau C, Rouzier R, Geyl C, et al. Predictive markers of chemoresistance in advanced stages epithelial ovarian carcinoma. *Gynecol Oncol*. Jan 2015;136(1):112-20. doi:10.1016/j.ygyno.2014.10.024

23.   Lloyd KL, Cree IA, Savage RS. Prediction of resistance to chemotherapy in ovarian cancer: a systematic review. *BMC Cancer*. Mar 11 2015;15:117. doi:10.1186/s12885-015-1101-8

24.   van Zyl B, Tang D, Bowden NA. Biomarkers of platinum resistance in ovarian cancer: what can we use to improve treatment. *Endocr Relat Cancer*. 05 2018;25(5):R303-R318. doi:10.1530/ERC-17-0336

25.   Batis N, Brooks JM, Payne K, Sharma N, Nankivell P, Mehanna H. Lack of predictive tools for conventional and targeted cancer therapy: Barriers to biomarker development and clinical translation. *Adv Drug Deliv Rev*. 09 2021;176:113854. doi:10.1016/j.addr.2021.113854

26.   Chen JS, Lan K, Hung MC. Strategies to target HER2/neu overexpression for cancer therapy. *Drug Resist Updat*. Jun 2003;6(3):129-36. doi:10.1016/s1368-7646(03)00040-2

27.   Spagnuolo A, Maione P, Gridelli C. The treatment of advanced non-small cell lung cancer harboring KRAS mutation: a new class of drugs for an old target-a narrative review. *Transl Lung Cancer Res*. Jun 2022;11(6):1199-1216. doi:10.21037/tlcr-21-948

28.   Marcus L, Lemery SJ, Keegan P, Pazdur R. FDA Approval Summary: Pembrolizumab for the Treatment of Microsatellite Instability-High Solid Tumors. *Clin Cancer Res*. 07 01 2019;25(13):3753-3758. doi:10.1158/1078-0432.CCR-18-4070

29.   Gosho M, Nagashima K, Sato Y. Study designs and statistical analyses for biomarker research. *Sensors (Basel)*. 2012;12(7):8966-86. doi:10.3390/s120708966

30.   Chatterjee SK, Zetter BR. Cancer biomarkers: knowing the present and predicting the future. *Future Oncol*. Feb 2005;1(1):37-50. doi:10.1517/14796694.1.1.37

31.   Ludwig JA, Weinstein JN. Biomarkers in cancer staging, prognosis and treatment selection. *Nat Rev Cancer*. Nov 2005;5(11):845-56. doi:10.1038/nrc1739

32.   Araujo P. Key aspects of analytical method validation and linearity evaluation. *J Chromatogr B Analyt Technol Biomed Life Sci*. Aug 01 2009;877(23):2224-34. doi:10.1016/j.jchromb.2008.09.030

33.   Dybkaer R. Vocabulary for use in measurement procedures and description of reference materials in laboratory medicine. *Eur J Clin Chem Clin Biochem*. Feb 1997;35(2):141-73.

34.   Feinberg M. Validation of analytical methods based on accuracy profiles. *J Chromatogr A*. Jul 27 2007;1158(1-2):174-83. doi:10.1016/j.chroma.2007.02.021

35.   Pojić M, Mastilović J, Majcen N. Robustness of the near infrared spectroscopy method determined using univariate and multivariate approach. *Food Chem*. Oct 01 2012;134(3):1699-705. doi:10.1016/j.foodchem.2012.03.104

36.   Borman PJ, Chatfield MJ, Damjanov I, Jackson P. Method ruggedness studies incorporating a risk based approach: a tutorial. *Anal Chim Acta*. Oct 10 2011;703(2):101-13. doi:10.1016/j.aca.2011.07.008

37.   O'Connor JP, Aboagye EO, Adams JE, et al. Imaging biomarker roadmap for cancer studies. *Nat Rev Clin Oncol*. 03 2017;14(3):169-186. doi:10.1038/nrclinonc.2016.162

38.   Panzeri MM, Losio C, Della Corte A, et al. Prediction of Chemoresistance in Women

Undergoing Neo-Adjuvant Chemotherapy for Locally Advanced Breast Cancer: Volumetric Analysis of First-Order Textural Features Extracted from Multiparametric MRI. *Contrast Media Mol Imaging*. 2018;2018:8329041. doi:10.1155/2018/8329041

39.   Rockall A, Munari A, Avril N. New ways of assessing ovarian cancer response: metabolic imaging and beyond. *Cancer Imaging*. Sep 28 2012;12:310-4. doi:10.1102/1470-7330.2012.9004

40.   Liu J, Lv H, Dong J, et al. Diffusion-Weighted Magnetic Resonance Imaging for Early Detection of Chemotherapy Resistance in Non-Small Cell Lung Cancer. *Med Sci Monit*. Aug 20 2019;25:6264-6270. doi:10.12659/MSM.914236

41.   Kyle SD, Law WP, Miles KA. Predicting tumour response. *Cancer Imaging*. Sep 23 2013;13(3):381-90. doi:10.1102/1470-7330.2013.9039

42.   Sulong S. Genetic aberrations in childhood acute lymphoblastic leukaemia: application of high-density single nucleotide polymorphism array. *Malays J Med Sci*. Jul 2010;17(3):5-12.

43.   Gerlinger M, Rowan AJ, Horswell S, et al. Intratumor heterogeneity and branched evolution revealed by multiregion sequencing. *N Engl J Med*. Mar 08 2012;366(10):883-892. doi:10.1056/NEJMoa1113205

44.   Zhang J, Späth SS, Marjani SL, Zhang W, Pan X. Characterization of cancer genomic heterogeneity by next-generation sequencing advances precision medicine in cancer treatment. *Precis Clin Med*. Jun 2018;1(1):29-48. doi:10.1093/pcmedi/pby007

45.   Hu L, Ru K, Zhang L, et al. Fluorescence in situ hybridization (FISH): an increasingly demanded tool for biomarker research and personalized medicine. *Biomark Res*. Feb 05 2014;2(1):3. doi:10.1186/2050-7771-2-3

46.   Martin V, Bernasconi B, Merlo E, et al. ALK testing in lung adenocarcinoma: technical aspects to improve FISH evaluation in daily practice. *J Thorac Oncol*. Apr 2015;10(4):595-602. doi:10.1097/JTO.0000000000000444

47.   Oldenhuis CN, Oosting SF, Gietema JA, de Vries EG. Prognostic versus predictive value of biomarkers in oncology. *Eur J Cancer*. May 2008;44(7):946-53. doi:10.1016/j.ejca.2008.03.006

48.   Sawyers CL. The cancer biomarker problem. *Nature*. Apr 03 2008;452(7187):548-52. doi:10.1038/nature06913

49.   Crea F, Nobili S, Paolicchi E, et al. Epigenetics and chemoresistance in colorectal cancer: an opportunity for treatment tailoring and novel therapeutic strategies. *Drug Resist Updat*. Dec 2011;14(6):280-96. doi:10.1016/j.drup.2011.08.001

50.   Hu ZZ, Huang H, Wu CH, et al. Omics-based molecular target and biomarker identification. *Methods Mol Biol*. 2011;719:547-71. doi:10.1007/978-1-61779-027-0_26

51.   Tainsky MA. Genomic and proteomic biomarkers for cancer: a multitude of opportunities. *Biochim Biophys Acta*. Dec 2009;1796(2):176-93. doi:10.1016/j.bbcan.2009.04.004

52.   Draghici S, Khatri P, Eklund AC, Szallasi Z. Reliability and reproducibility issues in DNA microarray measurements. *Trends Genet*. Feb 2006;22(2):101-9. doi:10.1016/j.tig.2005.12.005

53.   Beard RE, Abate-Daga D, Rosati SF, et al. Gene expression profiling using nanostring digital RNA counting to identify potential target antigens for melanoma immunotherapy. *Clin Cancer Res*. Sep 15 2013;19(18):4941-50. doi:10.1158/1078-0432.CCR-13-1253

54.   Godoy PM, Barczak AJ, DeHoff P, et al. Comparison of Reproducibility, Accuracy, Sensitivity, and Specificity of miRNA Quantification Platforms. *Cell Rep*. 12 17 2019;29(12):4212-4222.e5. doi:10.1016/j.celrep.2019.11.078

55.   Lohmann S, Herold A, Bergauer T, et al. Gene expression analysis in biomarker research and early drug development using function tested reverse transcription quantitative real-time PCR

assays. *Methods*. Jan 2013;59(1):10-9. doi:10.1016/j.ymeth.2012.07.003

56.   Dou Y, Lv Y, Zhou X, et al. Antibody-sandwich ELISA analysis of a novel blood biomarker of CST4 in gastrointestinal cancers. *Onco Targets Ther*. 2018;11:1743-1756. doi:10.2147/OTT.S149204

57.   Taylor SC, Nadeau K, Abbasi M, Lachance C, Nguyen M, Fenrich J. The Ultimate qPCR Experiment: Producing Publication Quality, Reproducible Data the First Time. *Trends Biotechnol*. 07 2019;37(7):761-774. doi:10.1016/j.tibtech.2018.12.002

58.   Hayden H, Ibrahim N, Klopf J, et al. ELISA detection of MPO-DNA complexes in human plasma is error-prone and yields limited information on neutrophil extracellular traps formed in vivo. *PLoS One*. 2021;16(4):e0250265. doi:10.1371/journal.pone.0250265

59.   Wang Z, Gerstein M, Snyder M. RNA-Seq: a revolutionary tool for transcriptomics. *Nat Rev Genet*. Jan 2009;10(1):57-63. doi:10.1038/nrg2484

60.   Gallego Romero I, Pai AA, Tung J, Gilad Y. RNA-seq: impact of RNA degradation on transcript quantification. *BMC Biol*. May 30 2014;12:42. doi:10.1186/1741-7007-12-42

61.   Kumar D, Bansal G, Narang A, Basak T, Abbas T, Dash D. Integrating transcriptome and proteome profiling: Strategies and applications. *Proteomics*. 10 2016;16(19):2533-2544. doi:10.1002/pmic.201600140

62.   Cervera J, Meseguer S, Mafe S. The interplay between genetic and bioelectrical signaling permits a spatial regionalisation of membrane potentials in model multicellular ensembles. *Sci Rep*. 10 12 2016;6:35201. doi:10.1038/srep35201

63.   Ramón Y Cajal S, Sesé M, Capdevila C, et al. Clinical implications of intratumor heterogeneity: challenges and opportunities. *J Mol Med (Berl)*. 02 2020;98(2):161-177. doi:10.1007/s00109-020-01874-2

64.   Raatz M, Shah S, Chitadze G, Brüggemann M, Traulsen A. The impact of phenotypic heterogeneity of tumour cells on treatment and relapse dynamics. *PLoS Comput Biol*. 02 2021;17(2):e1008702. doi:10.1371/journal.pcbi.1008702

65.   Koshkin V, Kochmann S, Sorupanathan A, et al. Cytometry of Reaction Rate Constant: Measuring Reaction Rate Constant in Individual Cells To Facilitate Robust and Accurate Analysis of Cell-Population Heterogeneity. *Anal Chem*. 03 2019;91(6):4186-4194. doi:10.1021/acs.analchem.9b00388

66.   McKinnon KM. Flow Cytometry: An Overview. *Curr Protoc Immunol*. 02 21 2018;120:5.1.1-5.1.11. doi:10.1002/cpim.40

67.   Walling MA, Shepard JR. Cellular heterogeneity and live cell arrays. *Chem Soc Rev*. Jul 2011;40(7):4049-76. doi:10.1039/c0cs00212g

68.   Robinson PK. Enzymes: principles and biotechnological applications. *Essays Biochem*. 2015;59:1-41. doi:10.1042/bse0590001

69.   Sunray M, Zurgil N, Shafran Y, Deutsch M. Determination of individual cell Michaelis-Menten constants. *Cytometry*. Jan 01 2002;47(1):8-16. doi:10.1002/cyto.10029

70.   Kubitscheck U, Pratsch L, Passow H, Peters R. Calcium pump kinetics determined in single erythrocyte ghosts by microphotolysis and confocal imaging. *Biophys J*. Jul 1995;69(1):30-41. doi:10.1016/S0006-3495(95)79875-7

71.   Afrimzon E, Zurgil N, Shafran Y, et al. Monitoring of intracellular enzyme kinetic characteristics of peripheral mononuclear cells in breast cancer patients. *Cancer Epidemiol Biomarkers Prev*. Feb 2004;13(2):235-41. doi:10.1158/1055-9965.epi-03-0153

72.   Blokh D, Stambler I, Afrimzon E, et al. The information-theory analysis of Michaelis-Menten constants for detection of breast cancer. *Cancer Detect Prev*. 2007;31(6):489-98.

doi:10.1016/j.cdp.2007.10.010

73.   Blokh D, Afrimzon E, Stambler I, et al. Breast cancer detection by Michaelis-Menten constants via linear programming. *Comput Methods Programs Biomed*. Mar 2007;85(3):210-3. doi:10.1016/j.cmpb.2006.11.003

74.   Bukowski K, Kciuk M, Kontek R. Mechanisms of Multidrug Resistance in Cancer Chemotherapy. *Int J Mol Sci*. May 02 2020;21(9)doi:10.3390/ijms21093233

75.   Vasiliou V, Vasiliou K, Nebert DW. Human ATP-binding cassette (ABC) transporter family. *Hum Genomics*. Apr 2009;3(3):281-90. doi:10.1186/1479-7364-3-3-281

76.   Xiao H, Zheng Y, Ma L, Tian L, Sun Q. Clinically-Relevant ABC Transporter for Anti-Cancer Drug Resistance. *Front Pharmacol*. 2021;12:648407. doi:10.3389/fphar.2021.648407

77.   Lebedeva IV, Pande P, Patton WF. Sensitive and specific fluorescent probes for functional analysis of the three major types of mammalian ABC transporters. *PLoS One*. 2011;6(7):e22429. doi:10.1371/journal.pone.0022429

78.   Koshkin V, Krylov SN. Single-cell-kinetics approach to compare multidrug resistance-associated membrane transport in subpopulations of cells. *Anal Chem*. Aug 2011;83(16):6132-4. doi:10.1021/ac201690t

79.   Koshkin V, Yang BB, Krylov SN. Kinetics of MDR transport in tumor-initiating cells. *PLoS One*. 2013;8(11):e79222. doi:10.1371/journal.pone.0079222

80.   Koshkin V, Ailles LE, Liu G, Krylov SN. Preservation of the 3D Phenotype Upon Dispersal of Cultured Cell Spheroids Into Monolayer Cultures. *J Cell Biochem*. 01 2017;118(1):154-162. doi:10.1002/jcb.25621

81.   Koshkin V, Bleker de Oliveira M, Peng C, et al. Spheroid-Based Approach to Assess the Tissue Relevance of Analysis of Dispersed-Settled Tissue Cells by Cytometry of the Reaction Rate Constant. *Anal Chem*. 07 2020;92(13):9348-9355. doi:10.1021/acs.analchem.0c01667

82.   Dzyubachyk O, Essers J, van Cappellen WA, et al. Automated analysis of time-lapse fluorescence microscopy images: from live cell images to intracellular foci. *Bioinformatics*. Oct 01 2010;26(19):2424-30. doi:10.1093/bioinformatics/btq434

83.   Wen C, Miura T, Voleti V, et al. 3DeeCellTracker, a deep learning-based pipeline for segmenting and tracking cells in 3D time lapse images. *Elife*. 03 30 2021;10doi:10.7554/eLife.59187

84.   Gomes CJ, Harman MW, Centuori SM, Wolgemuth CW, Martinez JD. Measuring DNA content in live cells by fluorescence microscopy. *Cell Div*. 2018;13:6. doi:10.1186/s13008-018-0039-z

85.   Chiang PJ, Wu SM, Tseng MJ, Huang PJ. Automated Bright Field Segmentation of Cells and Vacuoles Using Image Processing Technique. *Cytometry A*. 10 2018;93(10):1004-1018. doi:10.1002/cyto.a.23595

86.   Koos K, Molnár J, Kelemen L, Tamás G, Horvath P. DIC image reconstruction using an energy minimization framework to visualize optical path length distribution. *Sci Rep*. 07 25 2016;6:30420. doi:10.1038/srep30420

87.   Buggenthin F, Marr C, Schwarzfischer M, et al. An automatic method for robust and fast cell detection in bright field images from high-throughput microscopy. *BMC Bioinformatics*. Oct 04 2013;14:297. doi:10.1186/1471-2105-14-297

88.   Essa E, Xie X. Phase contrast cell detection using multilevel classification. *Int J Numer Method Biomed Eng*. 02 2018;34(2)doi:10.1002/cnm.2916

89.   Yeh CJ, Hsi BL, Faulk WP. Propidium iodide as a nuclear marker in immunofluorescence. II. Use with cellular identification and viability studies. *J Immunol Methods*. 1981;43(3):269-75.

doi:10.1016/0022-1759(81)90174-5

90.   Koshkin V, De Oliveira MB, Peng C, et al. Multi-drug-resistance efflux in cisplatin-naive and cisplatin-exposed A2780 ovarian cancer cells responds differently to cell culture dimensionality. *Mol Clin Oncol*. Aug 2021;15(2):161. doi:10.3892/mco.2021.2323

91.   Schindelin J, Arganda-Carreras I, Frise E, et al. Fiji: an open-source platform for biological-image analysis. *Nat Methods*. Jun 28 2012;9(7):676-82. doi:10.1038/nmeth.2019

92.   Tinevez JY, Perry N, Schindelin J, et al. TrackMate: An open and extensible platform for single-particle tracking. *Methods*. 02 15 2017;115:80-90. doi:10.1016/j.ymeth.2016.09.016

93.   Schmidt U, Weigert M, Broaddus C, Myers G. Cell Detection with Star-Convex Polygons. Springer International Publishing; 2018:265-273.

94.   Chan LL, Smith T, Kumph KA, et al. A high-throughput AO/PI-based cell concentration and viability detection method using the Celigo image cytometry. *Cytotechnology*. Oct 2016;68(5):2015-25. doi:10.1007/s10616-016-0015-x

95.   Chen J, Xu Y, Lv X, Lai X, Zeng S. Super-resolution differential interference contrast microscopy by structured illumination. *Opt Express*. Jan 14 2013;21(1):112-21. doi:10.1364/OE.21.000112

96.   Yin Z, Kanade T, Chen M. Understanding the phase contrast optics to restore artifact-free microscopy images for segmentation. *Med Image Anal*. Jul 2012;16(5):1047-62. doi:10.1016/j.media.2011.12.006

97.   White JG, Amos WB, Fordham M. An evaluation of confocal versus conventional imaging of biological structures by fluorescence light microscopy. *J Cell Biol*. Jul 1987;105(1):41-8. doi:10.1083/jcb.105.1.41

98.   Sharma P, Lam VK, Raub CB, Chung BM. Tracking Single Cells Motility on Different Substrates. *Methods Protoc*. Aug 04 2020;3(3)doi:10.3390/mps3030056

99.   Anorma C, Hedhli J, Bearrood TE, et al. Surveillance of Cancer Stem Cell Plasticity Using an Isoform-Selective Fluorescent Probe for Aldehyde Dehydrogenase 1A1. *ACS Central Science*. 2018/08/22 2018;4(8):1045-1055. doi:10.1021/acscentsci.8b00313

100.   Bearrood TE, Aguirre-Figueroa G, Chan J. Rational Design of a Red Fluorescent Sensor for ALDH1A1 Displaying Enhanced Cellular Uptake and Reactivity. *Bioconjugate Chemistry*. 2020/02/19 2020;31(2):224-228. doi:10.1021/acs.bioconjchem.9b00723

101.   Chang TK, Waxman DJ. Enzymatic analysis of cDNA-expressed human CYP1A1, CYP1A2, and CYP1B1 with 7-ethoxyresorufin as substrate. *Methods Mol Biol*. 2006;320:85-90. doi:10.1385/1-59259-998-2:85

102.   Muallem MZ, Braicu I, Nassir M, Richter R, Sehouli J, Arsenic R. ERCC1 expression as a predictor of resistance to platinum-based chemotherapy in primary ovarian cancer. *Anticancer Res*. Jan 2014;34(1):393-9.

103.   Guengerich FP. Cytochrome p450 and chemical toxicology. *Chem Res Toxicol*. Jan 2008;21(1):70-83. doi:10.1021/tx700079z

104.   Sangar MC, Bansal S, Avadhani NG. Bimodal targeting of microsomal cytochrome P450s to mitochondria: implications in drug metabolism and toxicity. *Expert Opin Drug Metab Toxicol*. Oct 2010;6(10):1231-51. doi:10.1517/17425255.2010.503955

105.   Nebert DW, Wikvall K, Miller WL. Human cytochromes P450 in health and disease. *Philos Trans R Soc Lond B Biol Sci*. Feb 2013;368(1612):20120431. doi:10.1098/rstb.2012.0431

106.   McDonnell AM, Dang CH. Basic review of the cytochrome p450 system. *J Adv Pract Oncol*. Jul 2013;4(4):263-8. doi:10.6004/jadpro.2013.4.4.7

107.   Rodriguez-Antona C, Ingelman-Sundberg M. Cytochrome P450 pharmacogenetics and

cancer. *Oncogene*. Mar 2006;25(11):1679-91. doi:10.1038/sj.onc.1209377

108.   Guengerich FP. Mechanisms of cytochrome P450 substrate oxidation: MiniReview. *J Biochem Mol Toxicol*. 2007;21(4):163-8. doi:10.1002/jbt.20174

109.   Kandel SE, Lampe JN. Role of protein-protein interactions in cytochrome P450-mediated drug metabolism and toxicity. *Chem Res Toxicol*. Sep 2014;27(9):1474-86. doi:10.1021/tx500203s

110.   Ortiz de Montellano PR. Hydrocarbon hydroxylation by cytochrome P450 enzymes. *Chem Rev*. Feb 2010;110(2):932-48. doi:10.1021/cr9002193

111.   Issa NT, Wathieu H, Ojo A, Byers SW, Dakshanamurthy S. Drug Metabolism in Preclinical Drug Development: A Survey of the Discovery Process, Toxicology, and Computational Tools. *Curr Drug Metab*. 2017;18(6):556-565. doi:10.2174/1389200218666170316093301

112.   Ung YT, Ong CE, Pan Y. Current High-Throughput Approaches of Screening Modulatory Effects of Xenobiotics on Cytochrome P450 (CYP) Enzymes. *High Throughput*. Sep 2018;7(4)doi:10.3390/ht7040029

113.   Anzenbacher P, Soucek P, Anzenbacherová E, et al. Presence and activity of cytochrome P450 isoforms in minipig liver microsomes. Comparison with human liver samples. *Drug Metab Dispos*. Jan 1998;26(1):56-9.

114.   Kimonen T, Juvonen RO, Alhava E, Pasanen M. The inhibition of CYP enzymes in mouse and human liver by pilocarpine. *Br J Pharmacol*. Feb 1995;114(4):832-6. doi:10.1111/j.1476-5381.1995.tb13279.x

115.   Burke MD, Thompson S, Weaver RJ, Wolf CR, Mayer RT. Cytochrome P450 specificities of alkoxyresorufin O-dealkylation in human and rat liver. *Biochem Pharmacol*. Aug 30 1994;48(5):923-36. doi:10.1016/0006-2952(94)90363-8

116.   Dhawan A, Parmar D, Dayal M, Seth PK. Cytochrome P450 (P450) isoenzyme specific dealkylation of alkoxyresorufins in rat brain microsomes. *Mol Cell Biochem*. Oct 1999;200(1-2):169-76. doi:10.1023/a:1007026800114

117.   Zeymer C, Hilvert D. Directed Evolution of Protein Catalysts. *Annu Rev Biochem*. 06 2018;87:131-157. doi:10.1146/annurev-biochem-062917-012034

118.   Michaelis L, Menten ML, Johnson KA, Goody RS. The original Michaelis constant: translation of the 1913 Michaelis-Menten paper. *Biochemistry*. Oct 2011;50(39):8264-9. doi:10.1021/bi201284u